GEOPHYSICS, VOL. 41, NO. 1 (FEBRUARY, 1976), P. 2-27, 8 FIGS.

SYNTHETIC SEISMOGRAMS: A FINITE-DIFFERENCE APPROACH

K. R. KELLY*, R. W. WARD‡, SVEN TREITEL*, AND R. M. ALFORD*

Recent interest in the extraction of fine detail from field seismograms has stimulated the search for numerical modeling procedures which can produce synthetic seismograms for complex subsurface geometries and for arbitrary source-receiver separations. Among the various techniques available for this purpose, the replacement of the two-dimensional wave equation by a suitable finite-difference representation offers distinct advantages. This approach is simple and may be readily implemented. It automatically accounts for the proper relative amplitudes of the various arrivals and includes the contributions of converted waves, Rayleigh waves, diffractions from faulted zones, and head waves.

Two computational schemes have been examined. For the so-called "homogeneous formulation," the standard boundary conditions between media of different elastic properties must be satisfied explicitly. In the case of the alternate "heterogeneous formulation", these elastic properties may be specified at each grid point of a finite-difference mesh, and the boundary conditions are satisfied implicitly. The proper simulation of the source requires special treatment for both cases.

Synthetic seismograms computed for several models of exploration interest serve to illustrate how the technique may help the interpreter. The examples also illustrate various implementational aspects of the finite-difference approach, which involve such phenomena as grid dispersion, artificial reflections from the edge of the model, and choice of spatial and temporal sampling increments.

INTRODUCTION

The synthetic seismogram has seen many years of widespread and successful application in geophysical prospecting. It found early use as a means to simulate the normal incidence reflectivity of a horizontally stratified medium and has been employed more recently to obtain the responses of subsurface structural and stratigraphic configurations (geologic models) of ever-increasing complexity. Indeed, the growing interest in numerical seismic modeling has led to a wide proliferation of methods of varying degrees of intricacy, accuracy, and implementational ease. Such efforts are spurred by the awareness that exact analytical solutions to the elastic wave equation do not exist for most subsurface configurations of exploration interest and that solutions to realistic models may be obtained only by approximate means.

Among the numerous techniques available for this purpose, the method of finite differences is particularly versatile. The two-dimensional partial differential equations of motion describing the propagation of stress waves in an elastic medium are approximated by suitable finite-difference equations, which can be solved on a discrete spatial grid by strictly numerical procedures. Since the finite-difference approach is based on the elastic wave equation without physical approximations, the method accounts not only for direct waves, primary reflected waves, and multiply reflected waves, but also for surface waves, head waves, converted reflected waves, diffracted waves, critically refracted waves, and waves ob-

Paper presented at the 44th Annual International SEG Meeting, November 13, 1974 in Dallas, Tex. Manuscript received by the Editor February 26, 1975; revised manuscript received July 18, 1975.
* Amoco Production Co., Tulsa, Okla. 74102.
‡ University of Texas at Dallas, Tex. 75080; formerly Amoco Production Co., Tulsa, Okla.

served in ray-theoretical shadow zones. Though already extensive, the literature in the finite-difference modeling of the wave equation has thus far not addressed itself in detail to the computation of synthetic seismograms of exploration interest. The present contribution indicates what can be accomplished in this regard.

Finite-difference methods can be classified in two broad categories: explicit and implicit. Explicit schemes for simulating the wave equation determine the motion for a space location at an advanced time exclusively from the motion already determined for previous times. Implicit schemes, on the other hand, simultaneously determine the motion at all space locations at an advanced time from known values at previous times through a matrix inversion technique. When applied to the wave equation, both schemes function as a "time-marching" procedure, in which the appropriate equations are solved recursively in time for the motion in a medium excited by a transient disturbance. Of the two categories, the explicit scheme is computationally the simpler and is employed here. Several alternate methods are discussed in Mitchell (1969).

The elastic medium may be considered as a collection of locally homogeneous lithologic regions, each characterized by constant values of the density and elastic parameters. Motion in each region may be described by an appropriate finite-difference representation for the elastic equations corresponding to that region. This approach will be called the "homogeneous" formulation. For this method, boundary conditions across all interfaces separating different regions must be satisfied explicitly. An alternative, "heterogeneous", approach incorporates the boundary conditions implicitly by constructing finite-difference representations for more general elastic equations, which are valid for a heterogeneous region. This approach makes it possible to associate different density and elastic parameter values with every grid point. Such a formulation provides the flexibility required to simulate a variety of complex subsurface geometries.

Our treatment begins with the more familiar homogeneous case, which leads us into a study of the more general heterogeneous case. This discussion is followed by a consideration of typical geologic models of exploration interest, and we compare the synthetic seismograms obtained (for similar subsurface geometries) by both the homogeneous and the heterogeneous formulations. Whenever a continuous medium is approximated by a discrete grid, the calculated seismic responses are dispersed, and the effect increases if the grid is made coarser. This so-called "grid dispersion" has a detrimental effect on the quality of the synthetic seismogram, as will be shown in some of the examples.

THE HOMOGENEOUS FORMULATION

The homogeneous formulation is not general in that it is intimately related to the model under consideration. We will demonstrate the formulation by consideration of a simple example consisting of two homogeneous layers separated by a plane, horizontal interface. The upper layer is bounded at the top by a plane, horizontal free surface. The model is bounded laterally and at depth by plane artificial interfaces as a result of the finite memory capacity of the computer.

For the sake of simplicity, we have chosen a model with a horizontal interface only: The method may be used for the case of vertical and dipping interfaces (Boore, 1970; Alterman and Loewenthal, 1970; Ottaviani, 1971). We restrict ourselves to a band-limited, pure compressional (*P*-) wave line source positioned in the interior of the upper layer. The time dependence of this source is assumed to be representable by the first derivative of the error density, or "Gaussian" function (Alford et al, 1974). Explicit finite-difference approximations for the wave equation and the associated boundary conditions for this case are given below. Our treatment is based on the work of Alterman and Karal (1968), who studied the case of a *P*-wave point source in a cylindrical coordinate system with azimuthal symmetry, and on further work by Ottaviani (1971), who solved the problem of a line source in one of two evenly welded quarter spaces by a similar approach in rectangular coordinates.

The equations of motion

Let x and z be the horizontal and vertical rectangular coordinates in a two-dimensional medium, and let the z-axis be positive downward. Under these conditions, two coupled, second-order, partial differential equations can be used to describe the motion of *P*-waves and vertically polarized shear (*SV*-) waves in a medium. The horizontally polarized shear (*SH*-) wave motion will not be treated here as it is uncoupled from the compressional (*P*-) and vertically polarized shear (*S*-) wave motion. The two equations of motion

are (Karal and Keller, 1959; White, 1965, p. 21)

$$\rho \frac{\partial^2 u}{\partial t^2} = (\lambda + 2\mu)\left(\frac{\partial^2 u}{\partial x^2} + \frac{\partial^2 w}{\partial x\, \partial z}\right) + \mu\left(\frac{\partial^2 u}{\partial z^2} - \frac{\partial^2 w}{\partial x\, \partial z}\right)$$

$$\rho \frac{\partial^2 w}{\partial t^2} = (\lambda + 2\mu)\left(\frac{\partial^2 u}{\partial x\, \partial z} + \frac{\partial^2 w}{\partial z^2}\right) + \mu\left(\frac{\partial^2 w}{\partial x^2} - \frac{\partial^2 u}{\partial x\, \partial z}\right). \quad (1)$$

Here u and w are the horizontal and vertical displacements, ρ is the density, t is the time, and λ and μ are the Lamé parameters of the particular medium.

A set of explicit, coupled finite-difference equations corresponding to equations (1) has been derived by Ottaviani (1971):

$$\begin{aligned} u(m, n, l+1) = {} & 2u(m, n, l) - u(m, n, l-1) \\ & + F^2[u(m+1, n, l) - 2u(m, n, l) + u(m-1, n, l)] \\ & + F^2(1-\gamma^2)[w(m+1, n+1, l) - w(m+1, n-1, l) \\ & - w(m-1, n+1, l) + w(m-1, n-1, l)]/4 \\ & + F^2\gamma^2[u(m, n+1, l) - 2u(m, n, l) + u(m, n-1, l)], \end{aligned}$$

and

$$\begin{aligned} w(m, n, l+1) = {} & 2w(m, n, l) - w(m, n, l-1) \\ & + F^2[w(m, n+1, l) - 2w(m, n, l) + w(m, n-1, l)], \\ & + F^2(1-\gamma^2)[u(m+1, n+1, l) - u(m+1, n-1, l) \\ & - u(m-1, n+1, l) + u(m-1, n-1, l)]/4 \\ & + F^2\gamma^2[w(m+1, n, l) - 2w(m, n, l) + w(m-1, n, l)], \end{aligned} \quad (2)$$

where $x = mh$, $z = nh$, and $t = l\Delta t$. The time step is Δt, h is the grid interval in both the x and z directions, and m, n, and l are defined to be integers. Furthermore, $\gamma = \beta/\alpha$ and denotes the ratio of the S-wave velocity β to the P-wave velocity α, where

$$\beta = \sqrt{\mu/\rho}$$

$$\alpha = \sqrt{(\lambda + 2\mu)/\rho}\,.$$

Finally, F is a parameter given by

$$F = \frac{\alpha\, \Delta t}{h}\,.$$

Equations (2) form an explicit scheme since they enable one to compute the displacements u and w at each spatial grid point at time step $(l + 1)$ exclusively in terms of the motion at the two previous time steps l and $(l - 1)$.

Stability condition

A physically meaningful numerical calculation requires that the finite-difference algorithm be stable, i.e., the difference between the exact and the numerical solutions of a finite-difference equation must remain bounded as the time index l increases, Δt remaining fixed for all m and n (Mitchell, 1969, p. 34). Alterman and Loewenthal (1970) have shown that the system of equations (2) is stable provided that

$$F = \frac{\alpha\, \Delta t}{h} \leq \left(1 + \frac{\beta^2}{\alpha^2}\right)^{-1/2}, \quad (3)$$

for all α and β. This inequality can also be written in the more revealing form

$$\Delta t \leq \frac{h}{(\alpha^2 + \beta^2)^{1/2}}\,,$$

which shows that the time increment Δt cannot be chosen arbitrarily but rather must obey a constraint imposed by the choice of a grid interval h as well as the values of the P- and S-wave velocities in the particular homogeneous layer.

Boundary conditions

The boundary conditions at the free surface require the stress to vanish, that is (Grant and West, 1965, p. 54),

$$(\alpha^2 - 2\beta^2)\frac{\partial u}{\partial x} + \alpha^2 \frac{\partial w}{\partial z} = 0$$

$$\frac{\partial u}{\partial z} + \frac{\partial w}{\partial x} = 0. \qquad (4)$$

The first equation refers to the normal stress and the second to the tangential stress. At a welded interface between two different elastic materials, boundary conditions require both the stress and the displacement to be continuous. For the plane horizontal interface at depth in the present model, this requirement gives (Grant and West, 1965),

$$\rho_1\left[\alpha_1^2 \frac{\partial w_1}{\partial z} + (\alpha_1^2 - 2\beta_1^2)\frac{\partial u_1}{\partial x}\right] = \rho_2\left[\alpha_2^2 \frac{\partial w_2}{\partial z} + (\alpha_2^2 - 2\beta_2^2)\frac{\partial u_2}{\partial x}\right]$$

$$\rho_1\beta_1^2\left[\frac{\partial u_1}{\partial z} + \frac{\partial w_1}{\partial x}\right] = \rho_2\beta_2^2\left[\frac{\partial u_2}{\partial z} + \frac{\partial w_2}{\partial x}\right]$$

$$w_1 = w_2,$$

$$u_1 = u_2. \qquad (5)$$

Here the subscripts 1 and 2 denote the media on opposite sides of the interface. The first two equations refer to continuity of normal and tangential stress, respectively, while the second two refer to the continuity of normal and tangential displacement. Following Alterman and Rotenberg (1969), we use one-sided differences to approximate normal derivatives and centered differences to approximate tangential derivatives. In this manner, we obtain at the free surface ($z = 0$) differenced boundary conditions corresponding to equations (4):

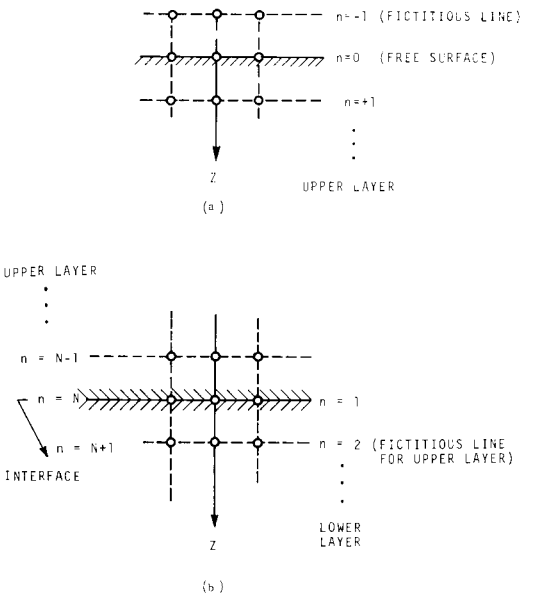

FIG. 1. Grid conventions: (a) at the free surface; (b) at the interface at depth, where the fictitious line of grid points is positioned in the lower (high velocity) layer (after Alterman and Karal, 1968).

where the subscript 1 identifies the upper layer. The index $n = -1$ arises because of the need to introduce a row of artificial grid points at a distance h above the free surface (Alterman and Karal, 1968) as illustrated in Figure 1a.

For the horizontal interface at depth, one places a row of artificial grid points at a distance h into the medium having the higher P- and S-wave velocities (Ottaviani, 1971). The case $\alpha_1 < \alpha_2$ and $\beta_1 < \beta_2$ is sketched in Figure 1b, where the subscript 2 denotes the lower layer. Following the grid indexing convention introduced by Alterman and Karal (1968), we write the four equations (5) for this case,

$$(\alpha_1^2 - 2\beta_1^2)\left[\frac{u_1(m+1, 0, l) - u_1(m-1, 0, l)}{2h}\right] + \alpha_1^2\left[\frac{w_1(m, 0, l) - w_1(m, -1, l)}{h}\right] = 0$$

$$\frac{u_1(m, 0, l) - u_1(m, -1, l)}{h} + \frac{w_1(m+1, 0, l) - w_1(m-1, 0, l)}{2h} = 0, \qquad (6)$$

$$\rho_1\left\{\alpha_1^2\left[\frac{w_1(m, N+1, l) - w_1(n, N, l)}{h}\right]\right.$$

$$\left. + (\alpha_1^2 - 2\beta_1^2)\left[\frac{u_1(m+1, N, l) - u_1(m-1, N, l)}{2h}\right]\right\}$$

$$= \rho_2\left\{\alpha_2^2\left[\frac{w_2(m, 2, l) - w_2(m, 1, l)}{h}\right]\right.$$

$$\left. + (\alpha_2^2 - 2\beta_2^2)\left[\frac{u_2(m+1, 1, l) - u_2(m-1, 1, l)}{2h}\right]\right\}$$

$$\rho_1\beta_1^2\left[\frac{u_1(m, N+1, l) - u_1(m, N, l)}{h} + \frac{w_1(m+1, N, l) - w_1(m-1, N, l)}{2h}\right]$$

$$= \rho_2\beta_2^2\left[\frac{u_2(m, 2, l) - u_2(m, 1, l)}{h} + \frac{w_2(m+1, 2, l) - w_2(m-1, 2, l)}{2h}\right]$$

$$u_1(m, N, l) = u_2(m, 1, l)$$

$$w_1(m, N, l) = w_2(m, 1, l). \qquad (7)$$

As shown in Figure 1b, the grid indexing convention places the interface at $n = N$ for the upper layer, while this same interface is at $n = 1$ for the lower layer. The artificial row of grid points for the upper layer corresponds to $n = 2$ for the lower layer.

Recently, Ilan and Loewenthal (1975) have reported that the method used to obtain finite-difference representations for the boundary conditions may create an upper stability limit with respect to the ratio β/α or, equivalently, with respect to Poisson's ratio. For the method used above, the upper limit for stability with regard to the free surface boundary condition is $\beta/\alpha = 0.35$. Corresponding results for the elastic-elastic boundary are not known at the present time.

The source

Inclusion of the source requires special consideration. Difficulties are encountered with numerical calculations in the vicinity of the source point. The problem may be avoided by subtracting the displacement due directly to the source from the total displacement in a rectangular region surrounding the source point. This procedure, in effect, inserts the source on the boundary of the rectangular region and avoids difficulties due to the source singularity. The direct source contribution is calculated analytically from the known solution for a source in an infinite region. The details of the analytical calculation are given in Appendix A. The method used for matching the displacements at the boundary of the rectangular region is essentially the same as that outlined by Alterman and Karal (1968).

The analytic expression for a compressional wave line source with a time variation taken to be the first derivative of a Gaussian is given in Appendix A [equation (A-15)]. The time variation of the source motion is similar to the first derivative of a Gaussian, but includes the added two-dimensional dispersion associated with a line source. It is tempting to use approximate or asymptotic source solutions for the sake of simplicity. We have found that the use of an analytic solution to the elastic wave equation, as opposed to an asymptotic approximation, results in a wavefront which propagates with the proper cylindrical symmetry and low amplitude "source noise". The source noise may be attributed to the fact that the

solution to the continuous analytical problem and the solution to the discrete finite-difference problem are not identical. The difference between the two is propagated through the grid as noise. A further advantage in using an analytical source field is that it permits a direct comparison with an analytical solution, if available (Alford et al, 1974).

Grid dispersion and edge reflections

Given the finite-difference equations, the boundary conditions, and the source, we may obtain the synthetic seismograms for two-dimensional geologic models of interest. However, such seismograms may contain several artifacts inherent to the finite-difference procedure, such as, grid dispersion and edge reflections.

Waves propagating on a discrete grid become progressively dispersed with increasing traveltime. This phenomenon, called grid dispersion, has been studied analytically as well as numerically (Boore, 1972; Alford et al, 1974). The dispersion increases in prominence as the grid interval h becomes larger. Grid dispersion produces a "normal" variation of velocity with frequency, that is, the higher signal frequencies are delayed relative to the lower signal frequencies and substantial "tailing" of the signal arises. As a rule of thumb, the number of grid points per wavelength at the upper half-power frequency of the source should be approximately ten or more (Alford et al, 1974) in order to satisfactorily limit the grid dispersion. All examples in this study satisfy this criteria except for one case in which it was violated to demonstrate the effects of grid dispersion.

The size of the finite-difference models is limited both laterally and vertically by the available computer memory. This restriction introduces artificial boundaries which produce undesired edge reflections. We are not aware of a fully satisfactory method to eliminate them, although we have investigated several possibilities. One approach, due to Lysmer and Kuhlemeyer (1969), has allowed us to attenuate the strength of such events, particularly in the case of P-waves. The method imposes viscous behavior on the artificial boundary, and much of the incident energy is mathematically "absorbed". For models with simple geometry, the edge reflections tend to have characteristic moveouts in the computed synthetic seismograms, and this characteristic permits their removal by filtering in the frequency-wavenumber domain. The edge reflection problem remains an active area of research.

HETEROGENEOUS FORMULATION

The homogeneous formulation is viable as long as the interfaces between media of different material properties remain horizontal or vertical planes. When interfaces become inclined or otherwise more geometrically complex, it becomes increasingly difficult to cope with the associated boundary conditions. In particular, one finds that each model requires extensive special purpose computer code, which more often than not will be inapplicable to a subsequent model of different complexity. These difficulties can be overcome by developing a finite-difference scheme for the general heterogeneous wave equation, which allows for spatial variations in the material properties. Boore (1972) applies this scheme to a scalar SH-wave propagation problem. The present treatment deals with a coupled, vector wave equation appropriate to P-SV wave propagation in a heterogeneous elastic medium. In the more general formulation, the Lamé parameters $\lambda(x,z)$ and $\mu(x,z)$ need no longer be constant in a particular medium but may vary from grid point to grid point. The scheme automatically accounts for the spatial variation in the elastic parameters across an interface whose geometrical complexity is limited only by the choice of the grid intervals Δx and Δz. The need to satisfy boundary conditions in the conventional manner has thus been obviated.

The second-order partial differential equations describing P-SV wave propagation in a two-dimensional medium in the rectangular coordinates x and z can be written (Kolsky, 1963, p. 11; Karal and Keller, 1959)

$$\rho \frac{\partial^2 u}{\partial t^2} = \frac{\partial}{\partial x}\left[\lambda\left(\frac{\partial u}{\partial x} + \frac{\partial w}{\partial z}\right) + 2\mu \frac{\partial u}{\partial x}\right] + \frac{\partial}{\partial z}\left[\mu\left(\frac{\partial w}{\partial x} + \frac{\partial u}{\partial z}\right)\right],$$

$$\rho \frac{\partial^2 w}{\partial t^2} = \frac{\partial}{\partial z}\left[\lambda\left(\frac{\partial u}{\partial x} + \frac{\partial w}{\partial z}\right) + 2\mu \frac{\partial w}{\partial z}\right] + \frac{\partial}{\partial x}\left[\mu\left(\frac{\partial w}{\partial x} + \frac{\partial u}{\partial z}\right)\right]. \quad (8)$$

These equations (8) reduce to the homogeneous equations (1) whenever ρ, λ, and μ are constant for a particular medium.

The assumption that the density ρ is constant throughout the model enables us to write the above equations as functions of the spatially varying P- and SV-wave velocities, i.e., λ and μ can be replaced by expressions in $\alpha(x,z)$ and $\beta(x,z)$. This assumption admittedly reduces the generality of our model; however, we avoid storing a third set of parameters in the computer memory.

We now develop a finite-difference scheme to approximate equations (8). The time differentials on the left-hand sides can be represented by the same centered differences that were used for the homogeneous case. On the right-hand side, however, we face the complication of differentiating terms which contain the spatially dependent elastic velocities. We must consider two types of terms that occur in equations (8), specifically, those having partial derivatives with respect to one spatial coordinate only and those containing partial derivatives with respect to both spatial variables (i.e., mixed derivatives).

Consider a term typical of the first type,

$$\frac{\partial}{\partial x}\left[\alpha^2(x,z)\frac{\partial u}{\partial x}\right]. \tag{9}$$

Let $\alpha^2(x,z)$ be replaced by its discrete value $\alpha^2(m,n)$ at the grid point (m,n). We define $\alpha^2(m,n)$ to be the average value of $\alpha^2(x,z)$ over a rectangle, of sides Δx and Δz, centered at the grid point $(m\Delta x, n\Delta z)$. Mitchell (1969, p. 22-25) and Boore (1972) discuss various approximations to (9). Experience thus far appears to indicate that many of these formulas yield comparable results. An approximation which has been found to perform satisfactorily is

$$\frac{\alpha^2(m+\frac{1}{2},n)[u(m+1,n,l)-u(m,n,l)]-\alpha^2(m-\frac{1}{2},n)[u(m,n,l)-u(m-1,n,l)]}{(\Delta x)^2}, \tag{10}$$

where the averages $\alpha^2(m+\frac{1}{2},n)$ and $\alpha^2(m-\frac{1}{2},n)$ are defined in the form,

$$\alpha^2(m\pm\tfrac{1}{2},n)=\frac{\alpha^2(m\pm1,n)+\alpha^2(m,n)}{2}. \tag{11}$$

Consider a term typical of a mixed derivative,

$$\frac{\partial}{\partial z}\left[\alpha^2(x,z)\frac{\partial}{\partial x}u(x,z,t)\right]\equiv\frac{\partial}{\partial z}[c(x,z,t)], \tag{12}$$

where the function $c(x,z,t)$ has been introduced for convenience. The right member of (12) may be approximated by the centered first-order difference,

$$\frac{\partial}{\partial z}[c(x,z,t)]\simeq\frac{c(m,n+1,l)-c(m,n-1,l)}{2\Delta z}. \tag{13}$$

Let

$$c(x,z,t)=\alpha^2(x,z)\frac{\partial}{\partial x}u(x,z,t)$$

be approximated by the centered first-order difference,

$$c(m,n,l)\simeq\alpha^2(m,n)\cdot\frac{u(m+1,n,l)-u(m-1,n,l)}{2\Delta x}. \tag{14}$$

Substitution of (14) into (13) yields the expression

$$\begin{aligned}\frac{\partial}{\partial z}\left[\alpha^2(x,z)\frac{\partial}{\partial x}u(x,z,t)\right]&\simeq\frac{1}{4\Delta x\,\Delta z}\{\alpha^2(m,n+1)\\&\cdot[u(m+1,n+1,l)-u(m-1,n+1,l)]\\&-\alpha^2(m,n-1)[u(m+1,n-1,l)-u(m-1,n-1,l)]\}.\end{aligned} \tag{15}$$

The other terms of (8) are handled in a like manner.

One finally obtains the two coupled finite-difference equations,

$$\frac{u(m, n, l+1) - 2u(m, n, l) + u(m, n, l-1)}{(\Delta t)^2}$$

$$= \frac{1}{\Delta x}\left\{\left[\frac{\alpha^2(m+1, n) + \alpha^2(m, n)}{2}\right]\left[\frac{u(m+1, n, l) - u(m, n, l)}{\Delta x}\right]\right.$$

$$\left. - \left[\frac{\alpha^2(m, n) + \alpha^2(m-1, n)}{2}\right]\left[\frac{u(m, n, l) - u(m-1, n, l)}{\Delta x}\right]\right\}$$

$$+ \frac{1}{2\Delta x}\left\{\alpha^2(m+1, n)\left[\frac{u(m+1, n+1, l) - u(m+1, n-1, l)}{2\Delta z}\right]\right.$$

$$\left. - \alpha^2(m-1, n)\left[\frac{u(m-1, n+1, l) - u(m-1, n-1, l)}{2\Delta z}\right]\right\}$$

$$- \frac{2}{2\Delta x}\left\{\beta^2(m+1, n)\left[\frac{w(m+1, n+1, l) - w(m+1, n-1, l)}{2\Delta z}\right]\right.$$

$$\left. - \beta^2(m-1, n)\left[\frac{w(m-1, n+1, l) - w(m-1, n-1, l)}{2\Delta z}\right]\right\}$$

$$+ \frac{1}{2\Delta z}\left\{\beta^2(m, n+1)\left[\frac{w(m+1, n+1, l) - w(m-1, n+1, l)}{2\Delta x}\right]\right.$$

$$\left. - \beta^2(m, n-1)\left[\frac{w(m+1, n-1, l) - w(m-1, n-1, l)}{2\Delta x}\right]\right\}$$

$$+ \frac{1}{\Delta z}\left\{\left[\frac{\beta^2(m, n+1) + \beta^2(m, n)}{2}\right]\left[\frac{u(m, n+1, l) - u(m, n, l)}{\Delta z}\right]\right.$$

$$\left. - \left[\frac{\beta^2(m, n) + \beta^2(m, n-1)}{2}\right]\left[\frac{u(m, n, l) - u(m, n-1, l)}{\Delta z}\right]\right\}$$

and

$$\frac{w(m, n, l+1) - 2w(m, n, l) + w(m, n, l-1)}{(\Delta t)^2}$$

$$= \frac{1}{2\Delta z}\left\{\alpha^2(m, n+1)\left[\frac{u(m+1, n+1, l) - u(m-1, n+1, l)}{2\Delta x}\right]\right.$$

$$\left. - \alpha^2(m, n-1)\left[\frac{u(m+1, n-1, l) - u(m-1, n-1, l)}{2\Delta x}\right]\right\}$$

$$+ \frac{1}{\Delta z}\left\{\left[\frac{\alpha^2(m, n+1) + \alpha^2(m, n)}{2}\right]\left[\frac{w(m, n+1, l) - w(m, n, l)}{\Delta z}\right]\right.$$

$$\left. - \left[\frac{\alpha^2(m, n) + \alpha^2(m, n-1)}{2}\right]\left[\frac{w(m, n, l) - w(m, n-1, l)}{\Delta z}\right]\right\}$$

$$- \frac{2}{2\Delta z}\left\{\beta^2(m, n+1)\left[\frac{u(m+1, n+1, l) - u(m-1, n+1, l)}{2\Delta x}\right]\right.$$

$$\left. - \beta^2(m, n-1)\left[\frac{u(m+1, n-1, l) - u(m-1, n-1, l)}{2\Delta x}\right]\right\}$$

$$+ \frac{1}{\Delta x}\left\{\left[\frac{\beta^2(m+1, n) + \beta^2(m, n)}{2}\right]\left[\frac{w(m+1, n, l) - w(m, n, l)}{\Delta x}\right]\right.$$

$$- \left[\frac{\beta^2(m, n) + \beta^2(m-1, n)}{2}\right]\left[\frac{w(m, n, l) - w(m-1, n, l)}{\Delta x}\right]\Bigg\}$$

$$+ \frac{1}{2\Delta x}\Bigg\{\beta^2(m+1, n)\left[\frac{u(m+1, n+1, l) - u(m+1, n-1, l)}{2\Delta z}\right]$$

$$- \beta^2(m-1, n)\left[\frac{u(m-1, n+1, l) - u(m-1, n-1, l)}{2\Delta z}\right]\Bigg\}. \qquad (16)$$

Equations (16) may be solved explicitly for the displacements $u(m,n,l+1)$ and $w(m,n,l+1)$ in terms of the previous displacements at time steps l and $l-1$. Although the above derivation was carried through for a rectangular grid with spacings Δx and Δz, the calculations for synthetic seismograms were all performed with the square grid $\Delta x = \Delta z = h$.

It must be emphasized that neither of the methods used to approximate the mixed derivatives (9) and (12) nor the velocity averaging convention (11) is unique. In fact, we have investigated several alternative explicit approximations of similar accuracy but find that they do not generally produce significantly different results.

In a homogeneous region, the heterogeneous finite-difference equations (16) reduce to the corresponding homogeneous equations (2). The two regimes differ only in the manner in which they treat regions in which there are velocity changes. The matching of boundary conditions at an interface takes place explicitly in the case of the homogeneous scheme, whereas it is implied in the case of the heterogeneous scheme. Both schemes yield very similar, but not identical, synthetic seismograms for a given subsurface model; this will be illustrated. We have been unable to explain these discrepancies to our own satisfaction but present some preliminary thoughts in Appendix B.

The source and its inclusion are treated as in the homogeneous case. This requires that the source be located in the interior of a homogeneous zone of dimensions at least as large as the source square.

We have not performed a detailed stability analysis of the heterogeneous formulation. Observations suggest that minimizing the homogeneous stability condition (3) over all grid points is sufficient for stability of the heterogeneous case.

The free surface boundary condition can be treated exactly as before, by the simple expedient of including an artificial row of grid points at a distance h above the top of the model. This will impose the stability limit with respect to Poisson's ratio mentioned previously.

SYNTHETIC SEISMOGRAMS

Synthetic seismograms computed by finite-difference techniques can aid in the understanding and the interpretation of wave patterns observed on field seismograms. The present approach is a complete numerical wave theory thus accounting for all motion in a two-dimensional elastic medium. The method will be illustrated by synthetic seismograms computed for a variety of subsurface geologic models. Simple models are treated first. These are followed by more complex models containing potential stratigraphic and structural hydrocarbon traps. The models to be considered are (1) a weathered layer, (2) a layer over a half-space, (3) a 90 degree corner embedded in a half-space, and (4) a reflection amplitude anomaly. For simplicity, the density is everywhere constant and Poisson's ratio is everywhere 0.25 in all the models considered. Ray-theoretical traveltimes are used to identify events on the synthetic seismograms.

In addition, synthetic seismograms computed by the homogeneous and heterogeneous algorithms will be compared for the 90 degree corner model, and the grid dispersion effect will be demonstrated for the model of a layer over a half-space.

The amplitudes of the synthetic seismograms have been scaled by a multiplicative constant chosen to make the weaker events easily visible. This causes the high-amplitude events to be clipped but maintains the correct relative amplitudes between events.

Weathered-layer model

The weathered-layer model consists of a low-velocity (2000 ft/sec) layer overlying a high-velocity (6000 ft/sec) half-space (Figure 2a). The resulting finite-difference synthetic seismograms for the vertical and in-line horizontal motion appear in Figures 2b and 2c, respectively.

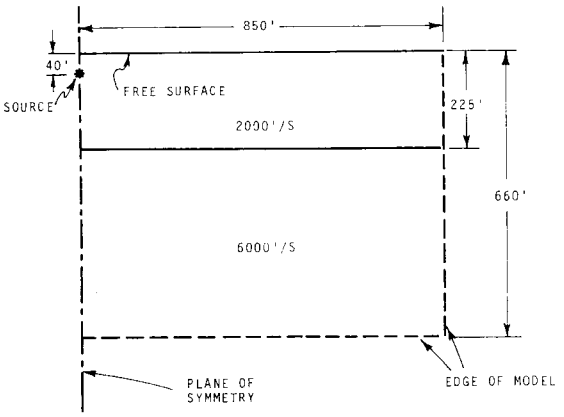

FIG. 2a. Geometry for a weathered-layer model.

The ray-theoretical traveltimes indicated on the seismograms accurately predict several early arriving waves. For small ranges (shot-receiver distances), the direct, reflected, and surface ghost reflected *P*-waves have similar waveforms. Beyond the critical reflection range (145 ft), the reflected *P*-wave exhibits a change in waveform and the *P*-head wave exists. The head wave travels with a greater apparent velocity than the direct and reflected waves and is visible before the *PP* reflection beyond a range of 300 ft; at a range of 585 ft, it appears before the direct *P*-wave. The amplitude of the head wave decays much faster with distance than the direct or reflected *P*-wave. The insert in Figure 2b shows the portion of the seismograms containing the head wave, with 18 db of additional gain.

Directly above the source there is no in-line horizontal motion (Figure 2c) from the direct, reflected, or surface reflected (ghost) *P*-wave. For a range greater than the total vertical travel path, these event are easily observable on the horizontal seismograms.

The shallow source in this model efficiently excites the Rayleigh wave. (In subsequent models a deep source is used to prevent Rayleigh-wave contamination of the seismograms.) An examination of the Rayleigh wave on the horizontal and vertical sections reveals the expected in-line, retrograde, elliptical particle motion. A Rayleigh-wave dispersion relation for a layer over a half-space (for a case with approximately the same velocity contrast as in the weathered-layer model) is given

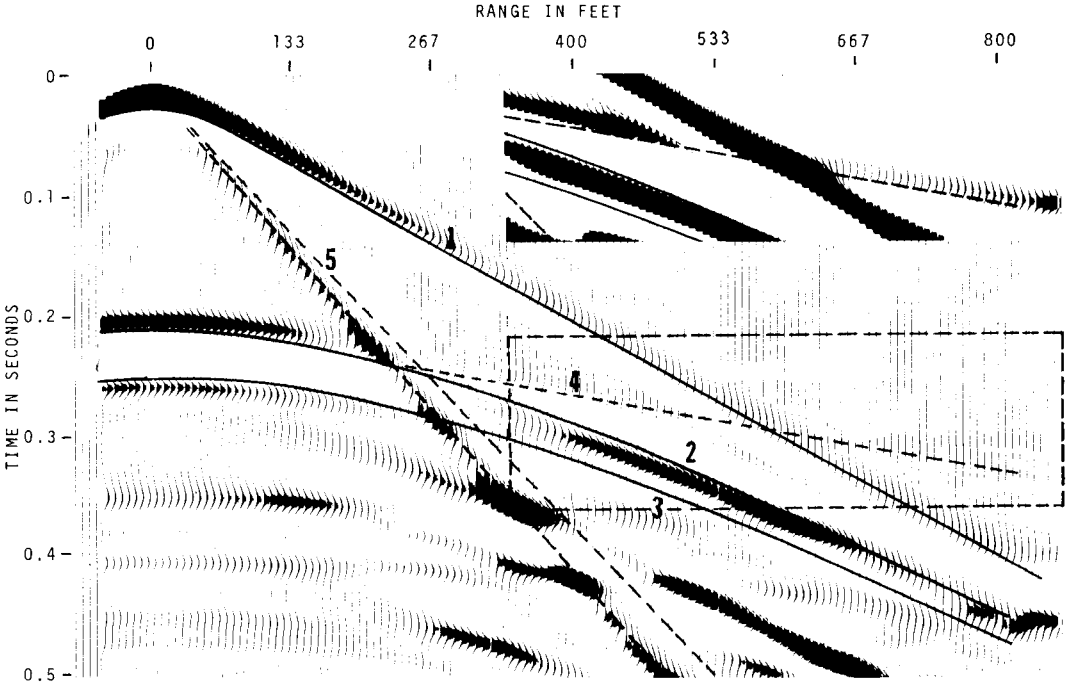

FIG. 2b. Vertical motion for the weathered-layer model. Theoretical arrival times are indicated for (1) direct *P*-wave, (2) *P*-wave reflection, (3) ghost *P*-wave reflection, (4) head wave, and (5) Rayleigh wave. The region in the dashed rectangle is shown in the inset with 18 db of additional gain.

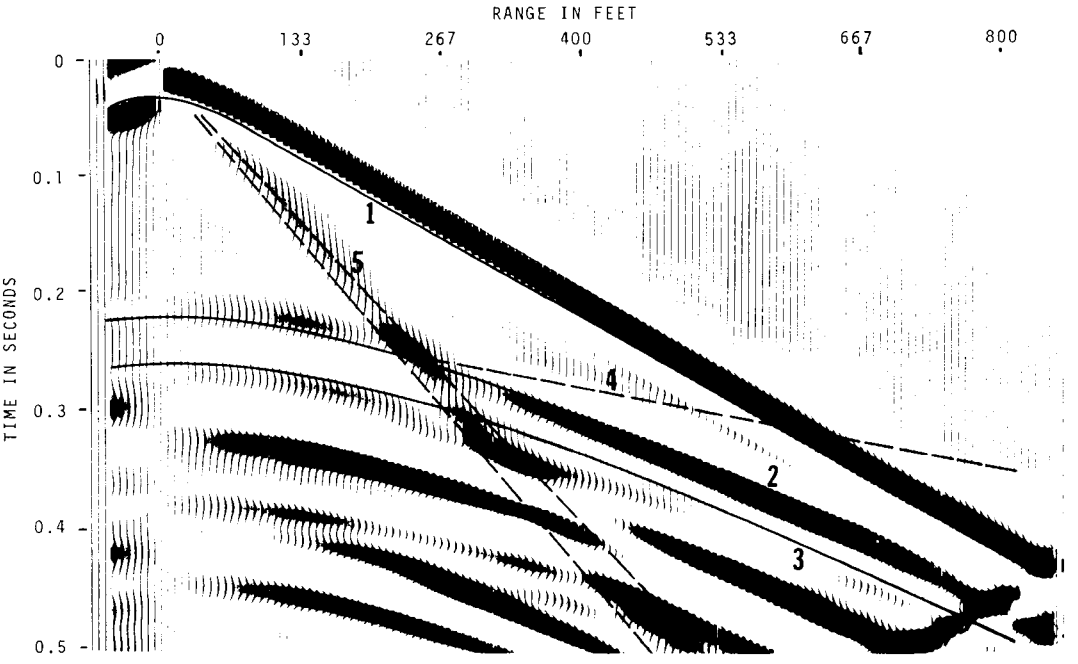

FIG. 2c. In-line horizontal motion for the weathered-layer model. Theoretical arrival times are indicated for (1) direct *P*-wave, (2) *P*-wave reflection, (3) ghost *P*-wave reflection, (4) head wave, and (5) Rayleigh wave.

by Tolstoy and Usdin (1953). The density contrast in the published relation does not correspond to the present situation. However, Rayleigh-wave velocity depends strongly on the velocity contrast and only weakly on the density contrast. The predicted group velocities of the various spectral components of the Rayleigh wave vary between 0.84 and 0.92 of the *S*-wave velocity of the upper layer; the lower frequency components travel at the lower velocity. The upper limit of the Rayleigh-wave velocity is identical to that of a half-space with the velocity of the layer. Arrival times for the upper and lower group velocities are displayed as dashed lines in Figures 2b and 2c. The computed Rayleigh-wave velocity is only slightly higher than the low-frequency velocity limit. A more detailed finite-difference investigation of Rayleigh-wave propagation can be found in Munasinghe and Farnell (1973).

Layer over a half-space

Grid dispersion and edge reflection effects will be illustrated with a model representing a layer over a half-space (Figure 3a). Both the vertical- and in-line horizontal-component seismograms are used to determine the wave mode (i.e., *P*- or *S*-wave arrival). The *P*-wave velocities are 6000 ft/sec in the layer and 9000 ft/sec in the half-space (Figure 3a) and are typical for a clastic sedimentary section. The synthetic seismograms for the vertical and horizontal motion are shown in Figures 3b and 3c, with ray-theoretical traveltimes indicated for selected arrivals.

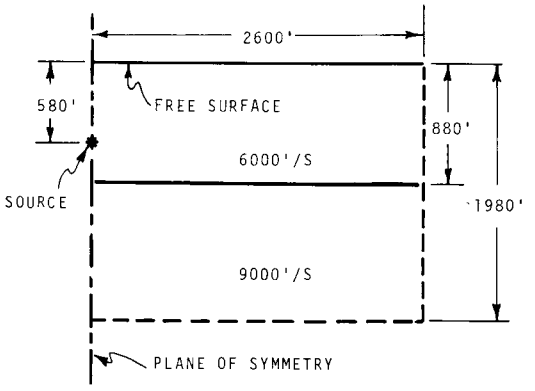

FIG. 3a. Geometry for the model of a layer over a half-space.

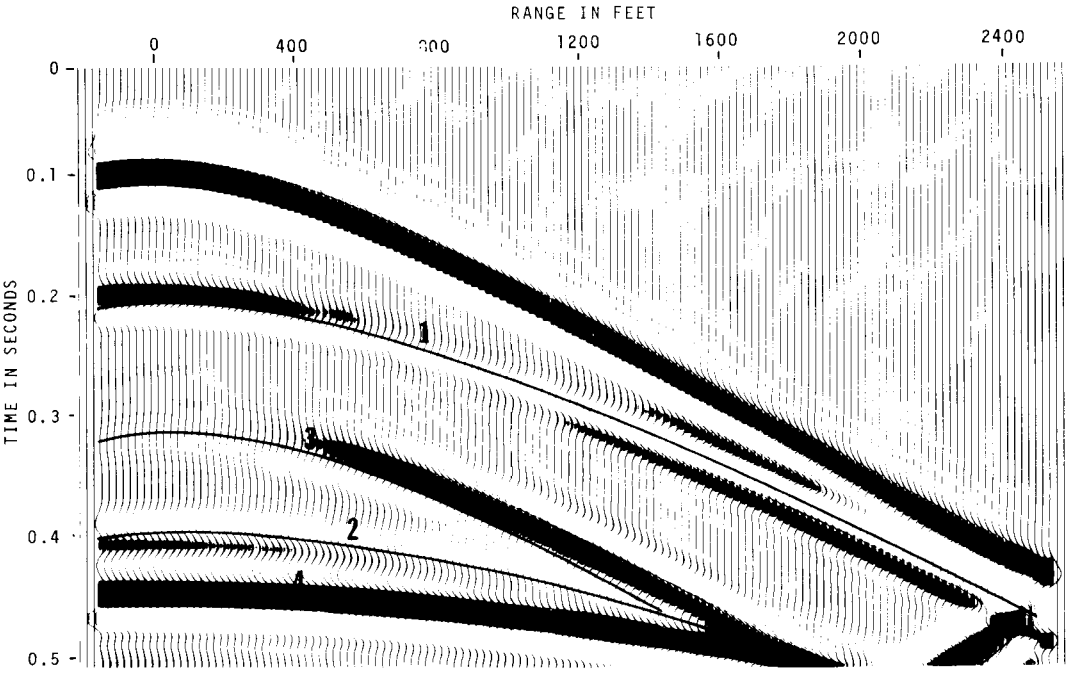

FIG. 3b. Vertical motion for the model of a layer over a half-space. Theoretical arrival times are indicated for (1) *P*-wave reflection, (2) ghost *P*-wave reflection, (3) *PS* reflection, and (4) *P*-wave bottom reflection. $G_p = 10.0$.

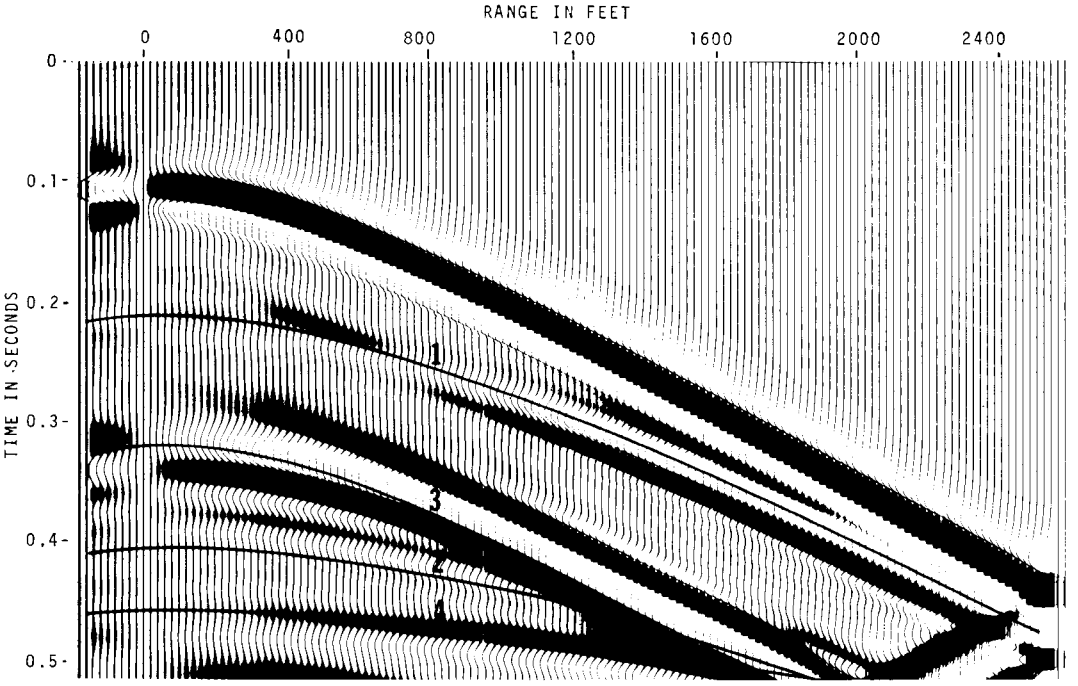

FIG. 3c. In-line horizontal motion for the model of a layer over a half-space. Theoretical arrival times are indicated for (1) *P*-wave reflection, (2) ghost *P*-wave reflection, (3) *PS* reflection, and (4) *P*-wave bottom reflection. $G_p = 10.0$.

The *P*-wave converted to an *S*-wave by reflection (*PS*-reflection) is distinctly visible on both the horizontal- and vertical-component seismograms. The shear motion at short ranges is nearly horizontal; thus, the *PS*-reflection is strongest at short ranges on the horizontal-motion seismogram. The broad low-frequency portion of the *PS*-wave reflection agrees with ray-theoretical traveltimes quite well; however, the higher frequency leading edge of this reflection propagates faster than expected.

The truncation of the model at the bottom and sides, required by the available computer memory, introduces spurious reflections in all models. The *P*-wave reflection from the bottom of the model is indicated in Figures 3b and 3c. The reflections from the right-hand side of the model appear in the synthetic seismograms as waves propagating to the left.

Grid dispersion is inherent when discrete grids are used to model wave propagation. The effect causes high-frequency components of the waves to propagate at velocities different from the low-frequency components. Unless grid dispersion is minimized by use of a sufficiently fine grid, artificial changes in waveform and spurious wavelets result. To illustrate this phenomenon, synthetic seismograms were computed with a high-frequency source obtained by doubling the frequency of each spectral component of the original source. This results in $G_p = 5.0$ rather than the more satisfactory value of $G_p = 10.0$ used in the two examples already discussed. Here G_p is defined as the number of grid points per *P*-wave wavelength at the upper half-power frequency of the source (Alford et al, 1974). The resulting vertical- and horizontal-component seismograms (Figures 3d and 3e) exhibit high-frequency ringing tails which follow each *P*-wave event (compare with Figures 3b and 3c). This effect is characteristic of grid dispersion associated with *P*-waves.

Grid dispersion will now be investigated in more detail using a model selected for computational convenience rather than geophysical significance. The model, shown in Figure 4a, consists of a half-space bounded by a free surface with both the source and observation points located at depth. Figure 4b shows the vertical motion for a grid size corresponding to $G_p = 5.0$ and Figure 4c shows the same result for $G_p = 10.0$.

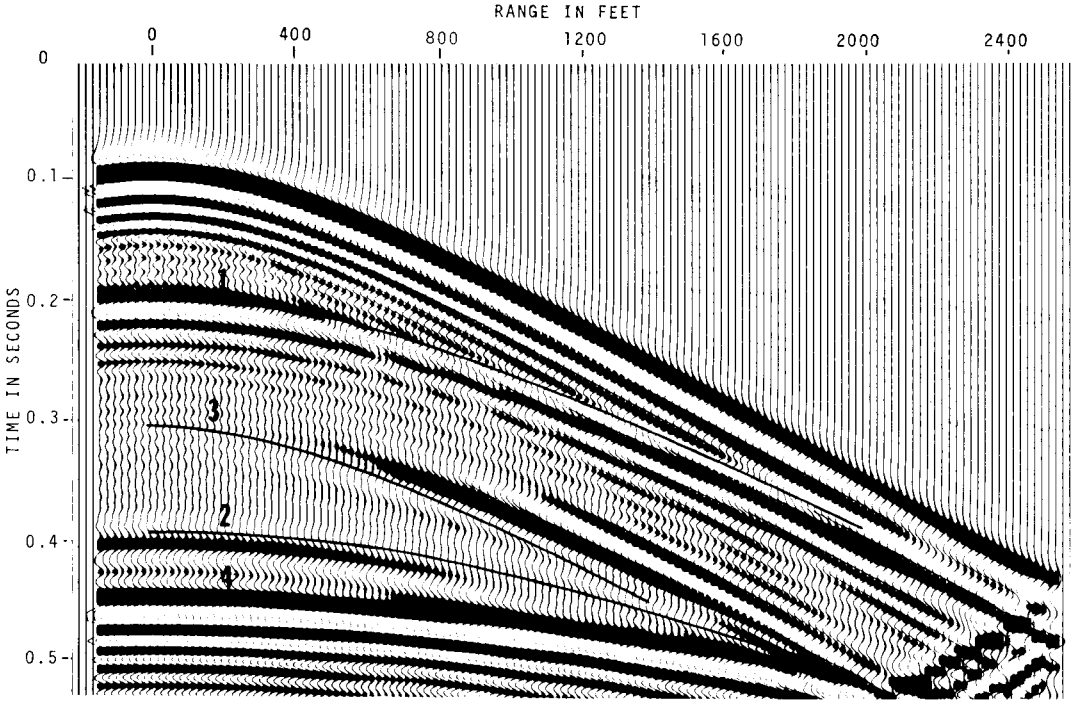

FIG. 3d. Vertical motion for the model of a layer over a half-space and a high-frequency source. Theoretical arrival times are indicated for (1) *P*-wave reflection, (2) ghost *P*-wave reflection, (3) *PS* reflection, and (4) *P*-wave bottom reflection. $G_p = 5.0$.

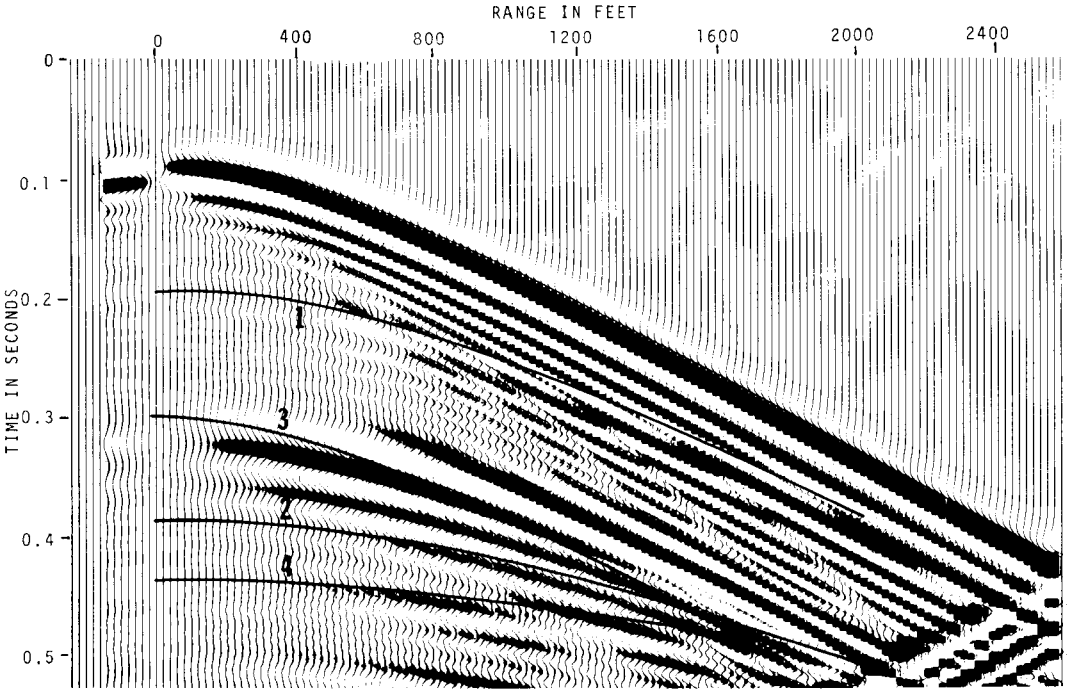

FIG. 3e. In-line horizontal motion for the model of a layer over a half-space and a high-frequency source. Theoretical arrival times are indicated for (1) *P*-wave reflection, (2) ghost *P*-wave reflection, (3) *PS* reflection, and (4) *P*-wave bottom reflection. $G_p = 5.0$.

Note that while ten grid points per wavelength appear adequate for prevention of appreciable dispersion in the *P*-wave events, the same criterion is not adequate for the *PS* wave. This is expected, since in any medium the wavelength of an *S*-wave is shorter than that of a *P*-wave of the same frequency. In this case, although the number of grid points per *P*-wavelength is 10.0, the number of grid points per *S*-wavelength (G_s) is 5.77.

Further examination and analysis indicates that dispersion of *S*-waves is quite different from that of *P*-waves in that the intermediate frequency components of the *S*-waves propagate faster than the low-frequency components. This results in a precursor on the *S*-wavelet, and the wavefront propagates at a velocity higher than expected.

Figure 4d shows comparative results for $G_s = 10.0$. This reduction in grid size appears sufficient to reduce the *S*-wave dispersion to an acceptable level, with no noticeable precursors and an arrival time very close to that predicted by ray theory.

90 degree-corner model

We next consider a model of a quarter-space embedded in a half-space; we here term this the "90 degree-corner" model (Figure 5a). This model will produce *P*- and *S*-wave diffractions from the corner. We compare solutions obtained by both the homogeneous and the heterogeneous formulations for $G_p = 10.0$. The vertical- and horizontal-component seismograms for the two formulations appear in Figures 5b through 5e. For both formulations, the traveltimes of the *P*-wave reflections and of both limbs of the *P*-wave diffraction agree

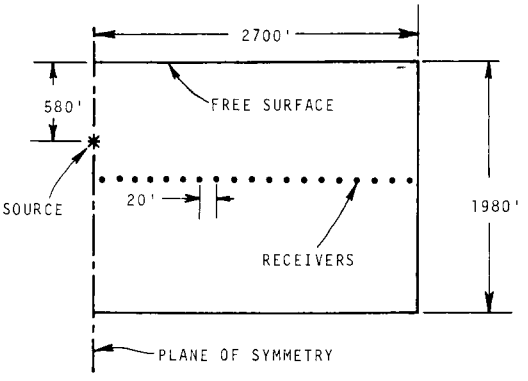

FIG. 4a. Geometry for a half-space model.

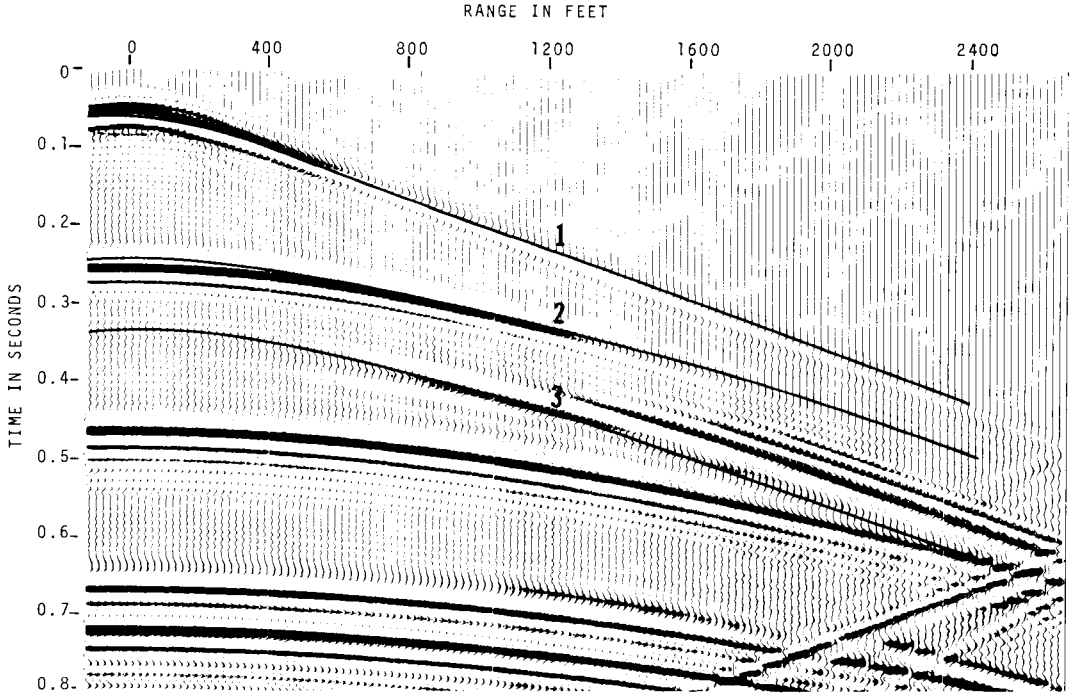

FIG. 4b. Grid dispersion for the half-space model with $G_p = 5.0$ (vertical motion). Theoretical arrival times are indicated for (1) direct *P*-wave, (2) *P*-wave reflection, and (3) *PS* reflection.

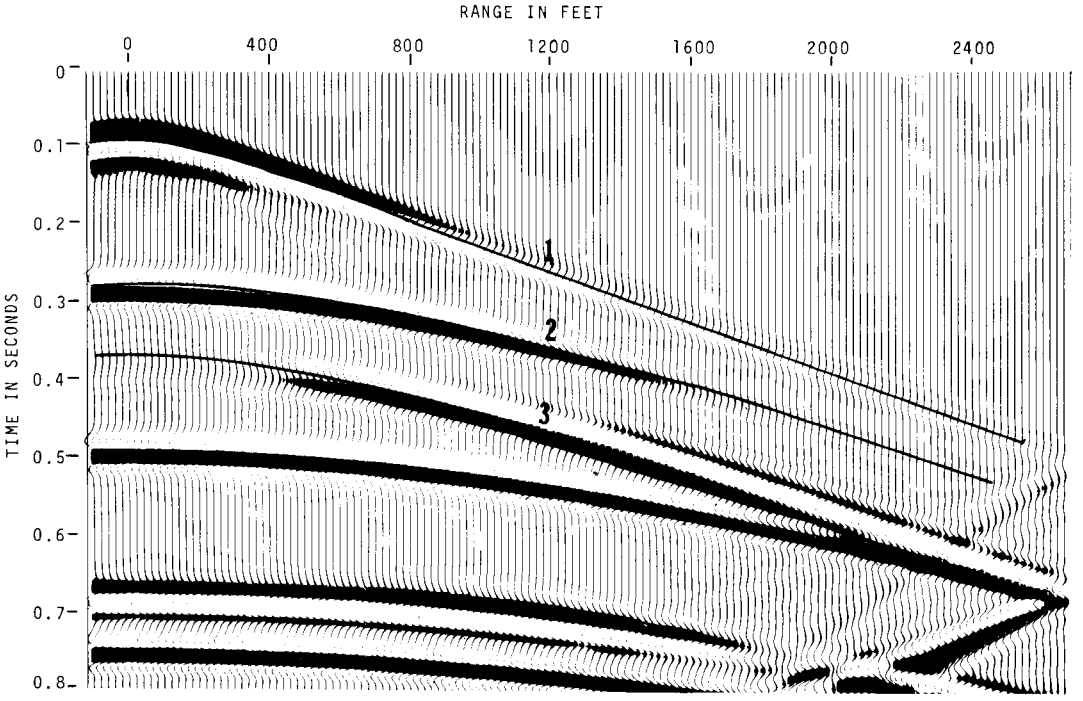

FIG. 4c. Grid dispersion for the half-space model with $G_d = 10.0$; $G_s = 5.77$ (vertical motion). Theoretical arrival times are indicated for (1) direct *P*-wave, (2) *P*-wave reflection, and (3) *PS* reflection.

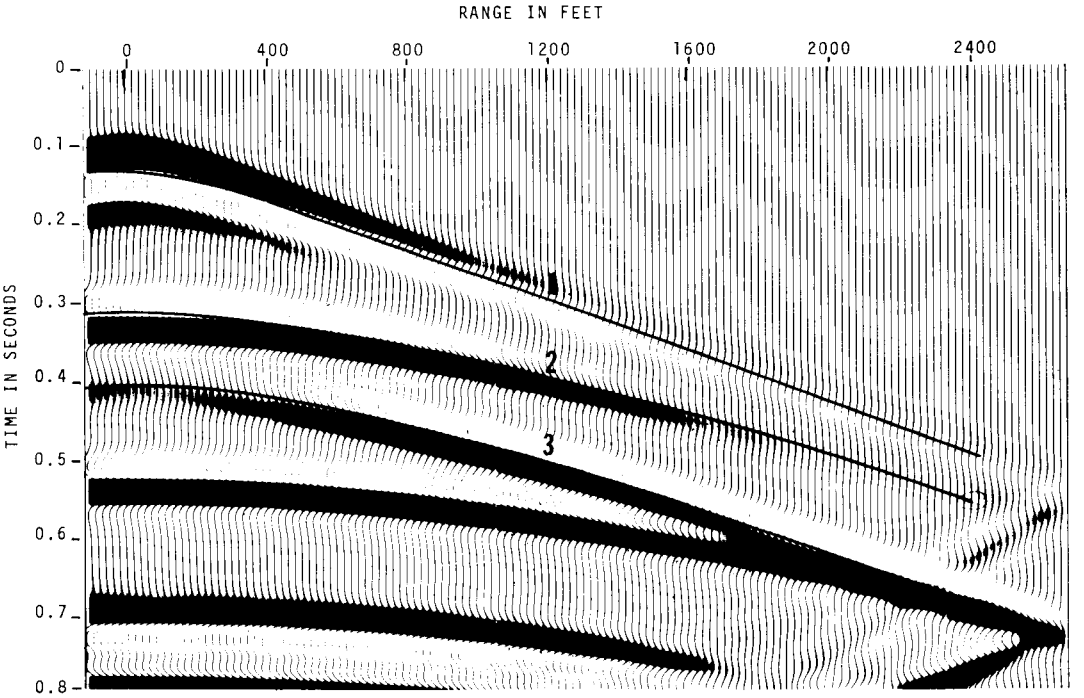

FIG. 4d. Grid dispersion for the half-space model with G_s = 10 (vertical motion). Theoretical arrival times are indicated for (1) direct *P*-wave, (2) *P*-wave reflection, and (3) *PS* reflection.

with ray theoretical values. The *PS* events appear to be traveling at higher velocities than predicted. In light of the above discussion, this is to be expected since the grid is not sufficiently fine to control *S*-wave dispersion. The amplitudes of the *P*-wave reflections obtained by the two formulations are essentially identical, whereas the *PS*-wave reflection amplitudes are stronger on the homogeneous formulation seismograms. The value of ν (defined in Appendix B) is 1.26 for this model, for which the heterogeneous solution should agree with theory to within 5 percent for plane *P*-wave reflections, and to within 10 percent for plane *PS*-wave reflections. The most apparent difference occurs for the *P*- and *S*-wave diffraction amplitudes, for which the homogeneous formulation produces significantly stronger diffractions than does the heterogeneous formulation. At present we do not know which formulation yields the more realistic amplitudes.

For *P*-waves reflected from the bottom of the model, a shadow zone exists between negative ranges of 248 and 1195 ft. The finite-difference method accounts for waves observed in this

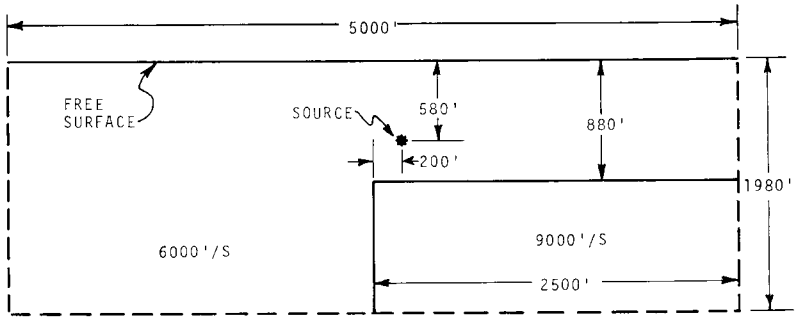

FIG. 5a. Geometry for a 90 degree corner model.

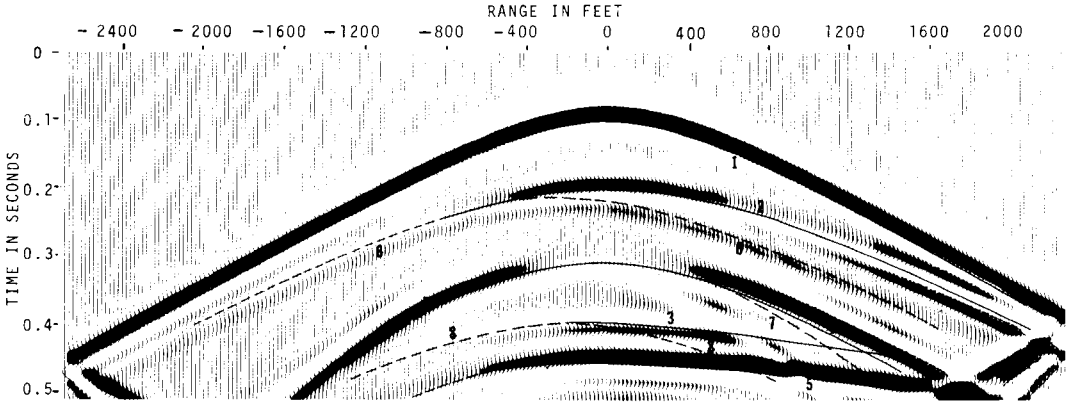

FIG. 5b. Vertical motion for the 90 degree corner model (homogeneous method). Theoretical arrival times are indicated for (1) direct *P*-wave, (2) *P*-wave reflection, (3) ghost *P*-wave reflection, (4) *PS* reflection, (5) *P*-wave bottom reflection, (6) *PP* diffraction, (7) *PS* diffraction, and (8) ghost *PP* diffraction.

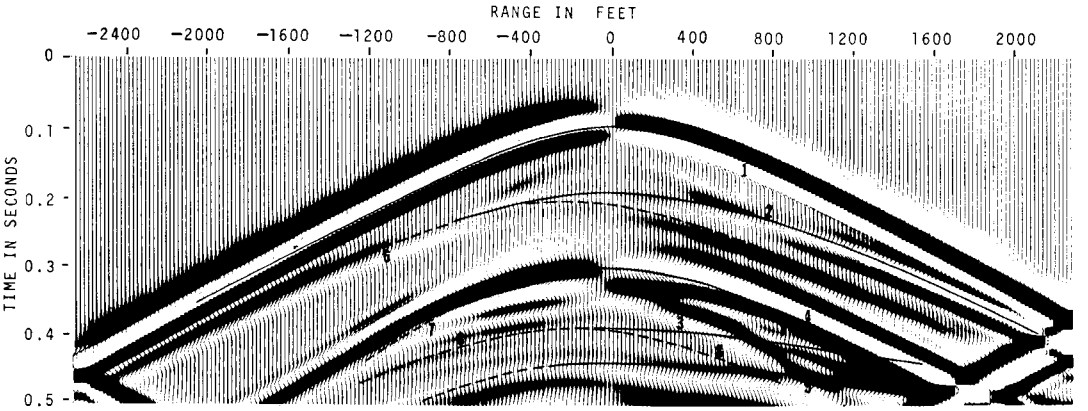

FIG. 5c. In-line horizontal motion for the 90 degree corner model (homogeneous method). Theoretical arrival times are indicated for (1) direct *P*-wave, (2) *P*-wave reflection, (3) ghost *P*-wave reflection, (4) *PS* reflection, (5) *P*-wave bottom reflection, (6) *PP* diffraction, (7) *PS* diffraction, and (8) ghost *PP* diffraction.

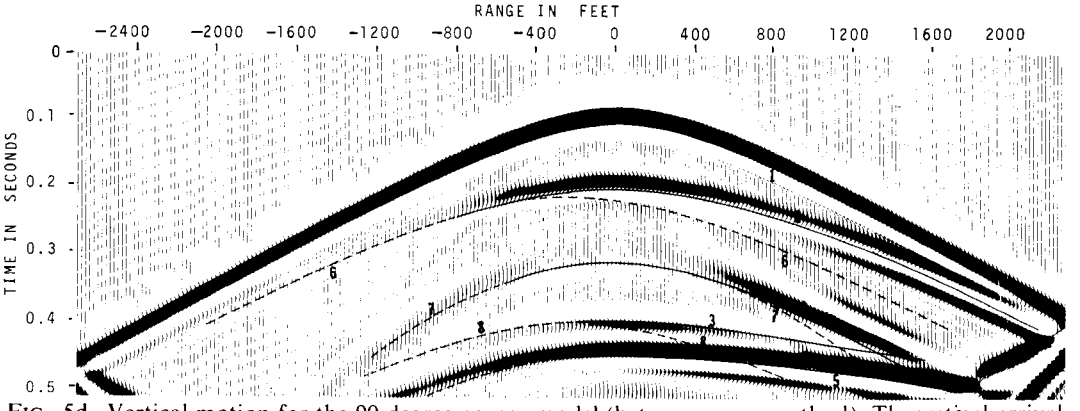

FIG. 5d. Vertical motion for the 90 degree corner model (heterogeneous method). Theoretical arrival times are indicated for (1) direct *P*-wave, (2) *P*-wave reflection, (3) ghost *P*-wave, (4) *PS* reflection, (5) *P*-wave bottom reflection, (6) *PP* diffraction, (7) *PS* diffraction, and (8) ghost *PP* diffraction.

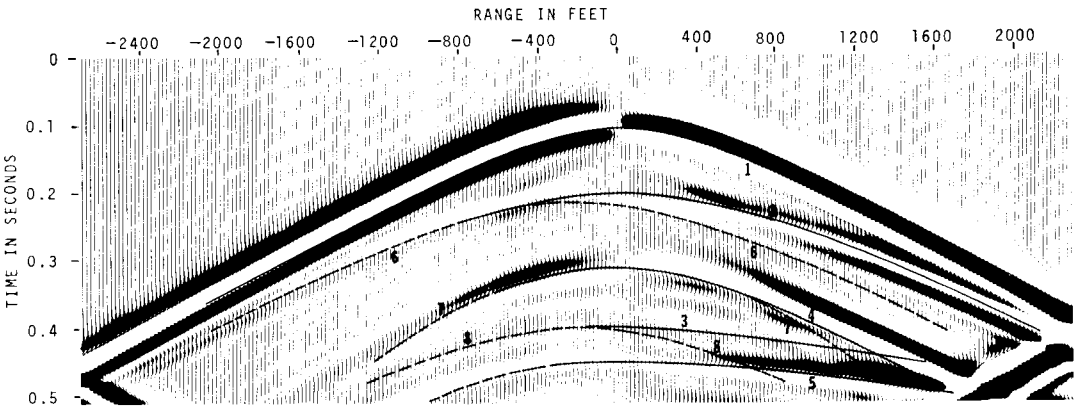

FIG. 5e. In-line horizontal motion for the 90 degree corner model (heterogeneous method). Theoretical arrival times are indicated for (1) direct *P*-wave, (2) *P*-wave reflection, (3) ghost *P*-wave reflection, (4) *PS* reflection, (5) *P*-wave bottom reflection, (6) *PP* diffraction, (7) *PS* diffraction, and (8) ghost *PP* diffraction.

shadow zone; the waves arise because the corner acts as a secondary source for these reflections. As an aid to visualization of the propagation of elastic waves in the presence of the 90 degree corner, a series of time "snapshots" of the vertical component of displacement at a given instant and at all ranges and depths computed are displayed in Figures 6a through 6f. The necessary calculations were made with the heterogeneous formulation. In the first snapshot, the direct *P*-wave from the line source appears with a cylindrical wavefront. *P*-waves, *S*-waves, head waves, and diffracted waves appear in the final snapshot. The intervening shapshots illustrate the increasing complexity of the interaction of the original *P*-wave with the 90 degree corner and with the edges of the model.

In the first snapshot, at a traveltime $t = 94$ msec (Figure 6a), a single *P*-wave appears with upward first motion above the source (white) and downward first motion below the source (black). At this time the wavefront has just reached the layer interface below the source.

The direct *P*-wave has reached the free surface in the snapshot at $t = 132$ msec (Figure 6b). Reflected and refracted waves have been produced by the *P*-wave which strikes the interface below the source.

At $t = 170$ msec, Figure 6c shows the direct *P*-wave reflected from the free surface. For the first time, the *S*-wave, refracted into the quarter-space, can be distinguished from the *P*-wave. Since the *PS*-wave diffraction has significant vertical motion when propagating horizontally, it is easily visible on the snapshot of vertical motion. The *PP*-wave, diffracted from the corner, cannot be distinguished since its motion is principally horizontal. The head wave generated by the *P*-wave which refracts into the high-velocity quarter-space and back into the low-velocity half-space exhibits a plane wavefront. This front connects the refracted *P*-wave event with the reflected *P*-wave event, in accordance with theoretical expectations.

The *PS*-reflection from the layer is visible for the first time in the snapshot at $t = 208$ msec (Figure 6d). The *PS*-head wave is also visible as a plane wavefront intersecting both the diffracted *PS*-wave and the refracted *P*-wave events.

The *P*-wave and *S*-wave reflections from the free surface separate in the snapshot at 246 msec (Figure 6e). The refracted *P*-wave reflects from the bottom of the model. The *P*-head wave, generated at the horizontal layer interface, is discernible just before the *P*-wave reflection.

A discontinuity in the wavefront slope of the *PP*-reflection from the bottom of the model is observed in the final snapshot at $t = 283$ msec (Figure 6f). This wave propagates along the vertical interface, passes the 90 degree corner, and establishes a ray-theoretical shadow zone.

Reflection amplitude anomaly model

The model to be considered represents a fluid-saturated 100 ft-thick sandstone layer which is embedded in shale. The physical parameters chosen (see Figures 7a and 7b) are typical of late Tertiary Gulf Coast reservoirs. In one case, the sandstone is completely saturated with brine (Figure

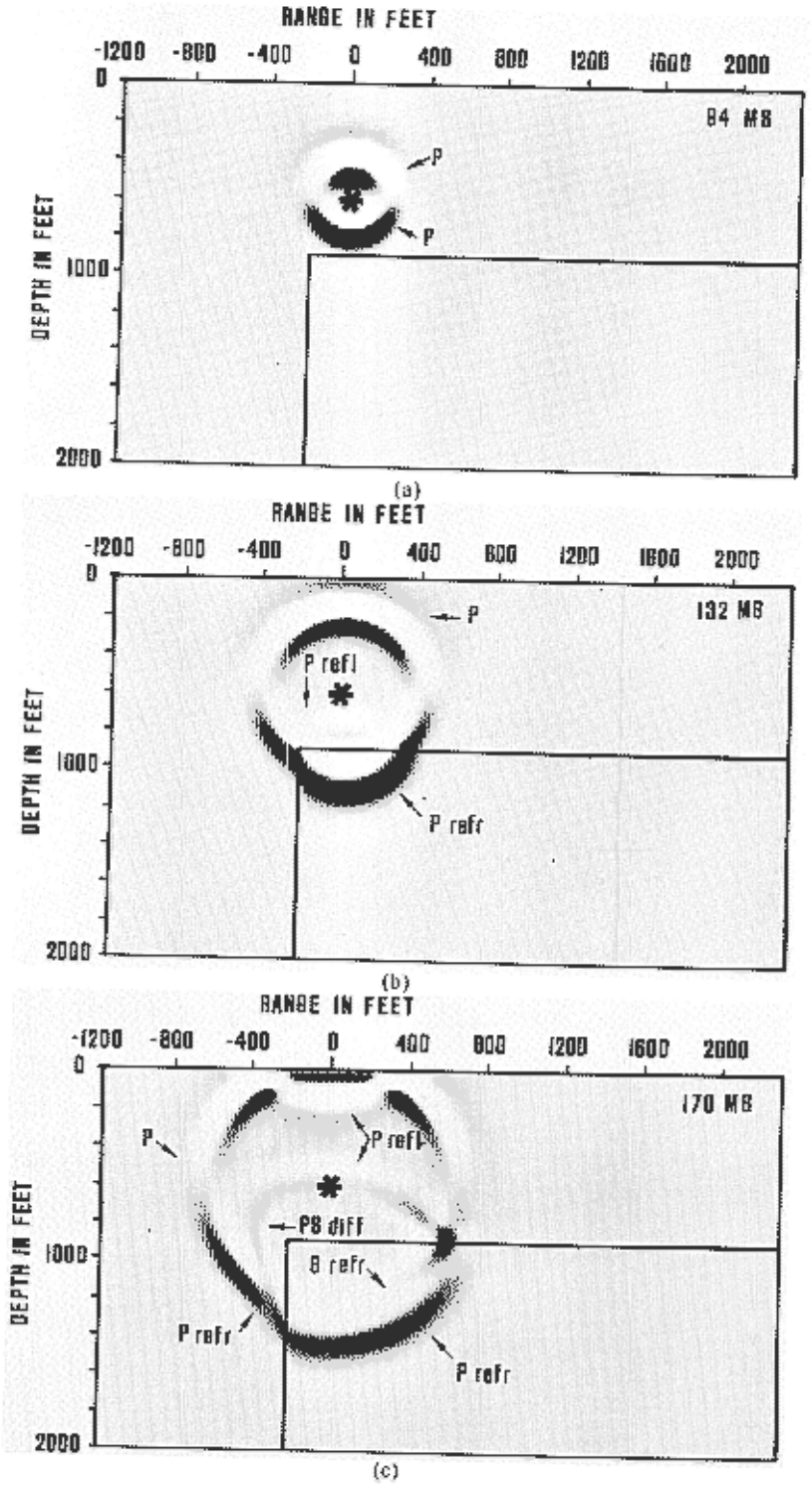

FIG. 6. "Snapshots" of the vertical components of displacement for the 90 degree corner after (a) 94 msec, (b) 132 msec, and (c) 170 msec.

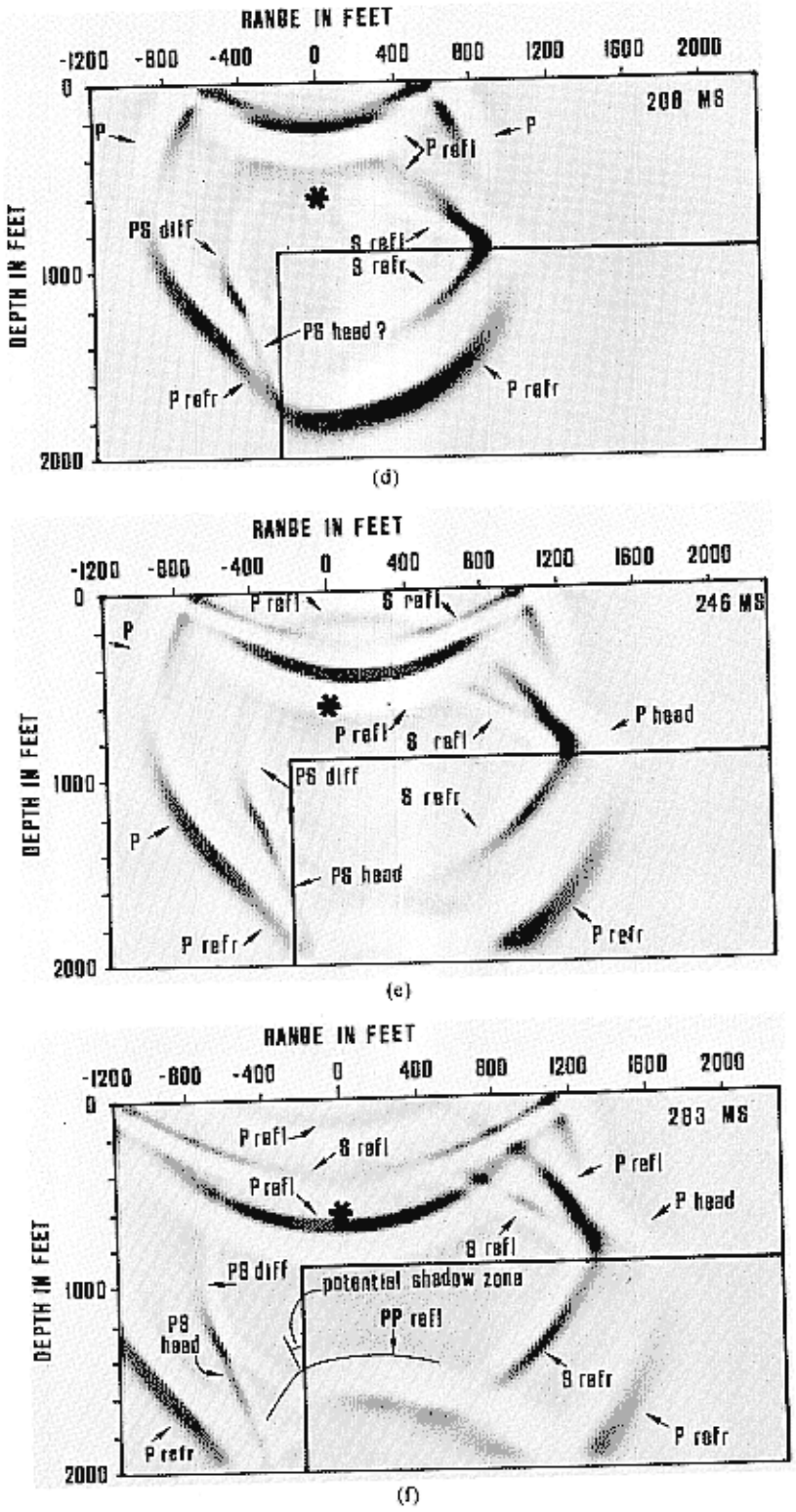

FIG. 6 (continued). "Snapshots" of the vertical component of displacement for the 90 degree corner after (d) 208 msec, (e) 246 msec, and (f) 283 msec.

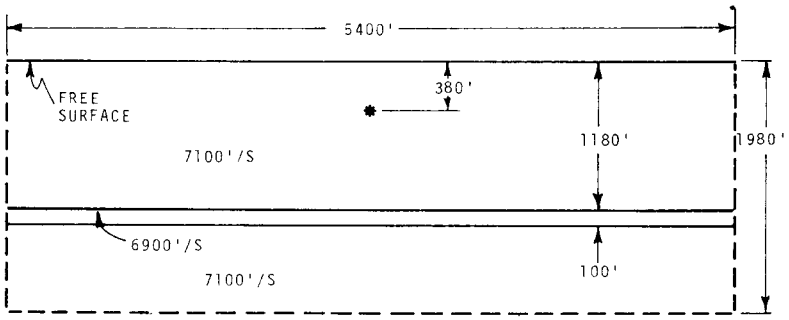

7a) and its P-wave velocity is almost equal to that of the shale. In the other case, the sandstone contains a zone of trapped gas (Figure 7b). Brine saturates the sandstone on either side of the gas zone. Since the presence of gas substantially lowers the P-wave velocity of the sandstone, an unusually large amplitude reflection appears above the gas zone.

The vertical-motion seismograms for the brine-saturated sandstone layer for $G_p = 10.0$ and $h = 20$ ft appear in Figure 7c. The low amplitude of the primary and surface ghost P-wave reflections is to be expected, since the velocity contrast between the shale and the brine-saturated sandstone is very small. The vertical-motion seismograms for the gas-saturated model for $G_p = 10.0$ and $h = 20$ ft appear in Figure 7d. The ray-theoretical considerations enable us to indicate the traveltimes of the P-wave reflections as well as the range limits for which the reflection raypaths strike the gas-saturated sandstone.

The reflections from the gas-saturated sandstone are significantly stronger than those from the brine-saturated sandstone. They are strongest in the center of the gas zone. The low-velocity, gas-saturated sandstone layer delays the waves which traverse it (including the reflections from the bottom of the model). These waves show a slight depression in their traveltime curve. We note that the events at ranges beyond the limits of the gas-saturated sandstone are now much stronger than corresponding reflection events from the purely brine-saturated layer (compare Figures 7c and 7d). The additional energy in these stronger events is due to the diffractions which arise at the interfaces between the gas- and brine-saturated zones. There is a weaker contribution to these events due to the reflection components from the interfaces between the brine-saturated zone and the shale host rock.

CONCLUDING REMARKS

The method of finite differences provides the geophysical interpreter with synthetic seismograms for quite arbitrary subsurface geologic models. From the examples we have given, it is evident that the resulting seismograms provide a fineness of detail difficult to obtain by alternate numerical procedures. Finite-difference techniques not only yield reliable arrival times for the

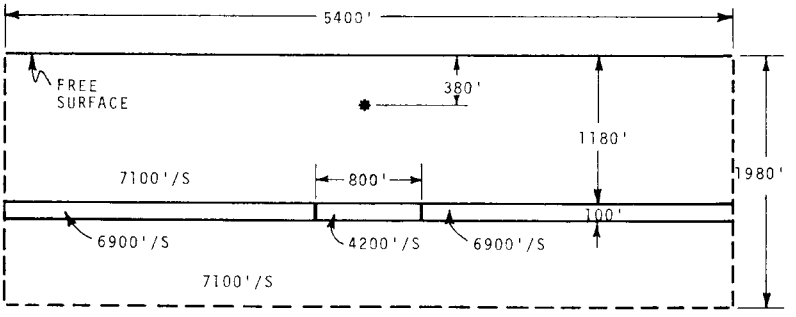

FIG. 7b. Geometry for a brine-gas model.

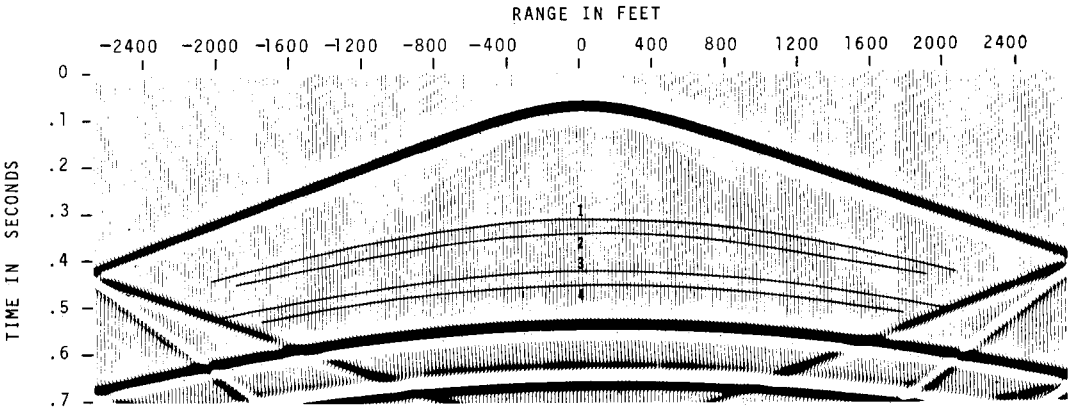

FIG. 7c. Vertical motion for the brine model. Theoretical arrival times are indicated for (1) *P*-wave reflection (top layer), (2) *P*-wave reflection (bottom layer), (3) ghost *P*-wave reflection (top layer), and (4) ghost *P*-wave reflection (bottom layer).

various seismic events, but also account for the variation in signal amplitude with subsurface elastic impedance contrasts and range. The complexity of our synthetic seismograms suggests that much diagnostic information present in field recordings may not be fully utilized in routine interpretations. For example, several of our models exhibit strong and easily identifiable "converted wave" (*PS*-wave) events. Such information, if discernible on real seismograms, should enhance the quality of the overall interpretation. Similar considerations may hold for the diffracted events and perhaps even for the head waves so clearly visible on some of our synthetic seismograms.

For the examples given, the velocity boundaries coincide with the grid points. We have considered models where this is not the case by using the heterogeneous formulation and have encountered no apparent difficulties. The present calculations were performed on an IBM 370/168 digital computer. Models exhibiting horizontal symmetry were run on a rectangular grid of 140 mesh points in the horizontal direction and 100 mesh points in the vertical direction (140 × 100). All others required a (250 × 100) grid. The spatial increment h was typically 20 ft. The time increment Δt cannot be chosen arbitrarily, since its value is governed by the stability limit condition [equation (3)]. For

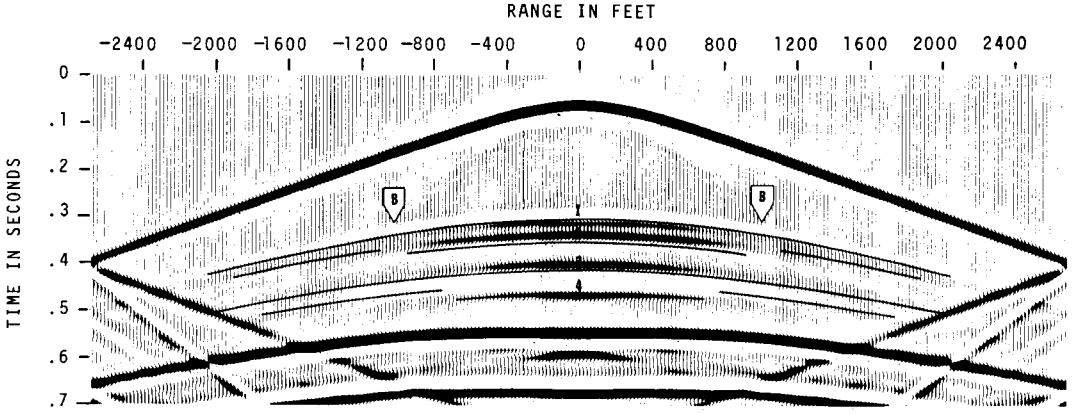

FIG. 7d. Vertical motion for the brine-gas model. Theoretical arrival times are indicated for (1) *P*-wave reflection (top layer), (2) *P*-wave reflection (bottom layer), (3) ghost *P*-wave reflection (top layer), and (4) ghost *P*-wave reflection (bottom layer). The ray theoretical limits of the gas reflection are indicated at B.

most cases, the value of Δt was in the neighborhood of 0.002 sec, and the calculations were performed for about 300 time steps. The resulting traces varied between 0.6 and 0.8 sec in length. An average model calculation required roughly 8 minutes of computer time in the central processing unit. It is, of course, desirable to extend the physical dimensions of the models in order to permit the simulation of subsurface geologic configuration of more realistic complexity and depth extent. The expense and core requirements of these calculations on a standard large-size computer rapidly become excessive as the number of grid points is increased. However, we have already established that a minicomputer with direct-access disk storage, dedicated to finite-difference simulation, can reduce costs to a more acceptable level.

In recent years, several other procedures for the calculation of synthetic seismograms have appeared in the literature. Among these we mention the finite-difference simulation of an approximation to the wave equation developed by Claerbout and his students at Stanford University (see, e.g., Claerbout and Johnson, 1971) and the method of finite elements (see, e.g., Strang and Fix, 1973). While Claerbout's techniques have been applied to the computer migration of seismic data, we are not aware of any exploration-oriented implementation of the finite-element approach. It is desirable that the various numerical simulation techniques be studied in terms of their relative advantages and limitations, a task which remains to be done.

The ability to obtain realistic synthetic seismograms for complex sub-surface geologic models should assist in the interpretation process. This is particularly true in view of the renewed emphasis on the diagnostic features of seismic amplitude variations. Finally, it is possible to envision the use of this modeling approach in an interactive computer environment, in which the interpreter makes successive guesses of the subsurface geologic model and compares the resulting synthetic seismograms with field recorded seismograms. We hope that our treatment will stimulate further activity in this intriguing area of research.

ACKNOWLEDGMENTS

We wish to thank L. Chobotuk and H. M. Williams for programming assistance. Thanks are due Amoco Production Co. for permission to publish this work.

REFERENCES

Aboudi, J., 1971, The motion excited by an impulsive source in an elastic half-space with a surface obstacle: Bull. Seism. Soc. Am., v. 61, p. 747–763.

Alford, R. M., Kelly, K. R., and Boore, D. M., 1974, Accuracy of finite-difference modeling of the acoustic wave equation: Geophysics, v. 39, p. 834–842.

Alterman, Z. S., and Karal, F. C., Jr., 1968, Propagation of elastic waves in layered media by finite-difference methods: Bull. Seism. Soc. Am., v. 58, p. 367–398.

Alterman, Z. S., and Loewenthal, D., 1970, Seismic waves in a quarter and three-quarter plane: Geophys. J. Roy. Astr. Soc., v. 20, p. 101–126.

Alterman, Z. S., and Rotenberg, A., 1969, Seismic waves in a quarter plane: Bull. Seism. Soc. Am., v. 59, p. 347–368.

Boore, D. M., 1970, Finite-difference solutions to the equations of elastic wave propagation, with applications to Love waves over dipping interfaces: Ph.D. thesis, M.I.T.

——— 1972, Finite-difference methods for seismic wave propagation in heterogeneous materials, *in* Methods in computational physics, v. 2: B. Alder, S. Fernbach, and M. Rotenberg, Eds., New York, Academic Press, p. 21–22.

Claerbout, J. F., and Johnson, A. G., 1971, Extrapolation of time-dependent waveforms along their path of propagation: Geophys. J. Roy. Astr. Soc., v. 26, p. 285–293.

Grant, F. S., and West, G. F., 1965, Interpretation theory in applied geophysics: New York, McGraw-Hill Book Co., Inc.

Gupta, R. N., 1966a, Reflection of elastic waves from a linear transition layer: Bull. Seism. Soc. Am., v. 56, p. 511–526.

——— 1966b, Reflection of plane elastic waves from transition layers with arbitrary variation of velocity and density: Bull. Seism. Soc. Am., v. 56, p. 633–642.

Ilan, A., and Loewenthal, D., 1975, Stability of finite-difference schemes due to boundary conditions in elastic media: Presented at the 37th EAEG Meeting, Bergen, June 18, 1975.

Karal, F. C., and Keller, J. B., 1959, Elastic wave propagation in homogeneous and inhomogeneous media: J. Acoust. Soc. Am., v. 31, p. 694–705.

Kolsky, H., 1963, Stress waves in solids: New York, Dover Publishing Co.

Lysmer, J., and Kuhlemeyer, R. L., 1969, Finite dynamic model for infinite media: J. Eng. Mech. Div., Proc. Am. Soc. Civil Eng., v. 95, p. 859–877.

Mitchell, A. R., 1969, Computational methods in partial differential equations: New York, John Wiley & Sons.

Morse, P. M., and Feshbach, H., 1953, Methods of theoretical physics: New York, McGraw-Hill Book Co., Inc.

Munasinghe, M., and Farnell, G. W., 1973, Finite-difference analysis of Rayleigh wave scattering at vertical discontinuities: J. Geophys. Res., v. 78, p. 2454–2466.

Ottaviani, M., 1971, Elastic wave propagation in two evenly-welded quarter-spaces: Bull. Seism. Soc. Am., v. 61, p. 1119–1152.

Strang, G., and Fix, G. J., 1973, An analysis of the finite-element method: Englewood Cliffs, N. J., Prentice-Hall, Inc.

Tolstoy, I., and Usdin, E., 1953, Dispersive properties of stratified elastic and liquid media—a ray theory: Geophysics, v. 18, p. 844–870.

White, J. E., 1965, Seismic waves: New York, McGraw-Hill Book Co., Inc.

APPENDIX A

INCLUSION OF A SINGULAR *P*-WAVE LINE SOURCE IN A FINITE-DIFFERENCE ALGORITHM

The inclusion of the desired type of singular line source in a discrete grid may be accomplished by reducing the original problem to three separate problems: The first two are source free and quite amenable to finite-difference treatment, while the third contains a source with a well-known analytical representation. A similar approach has been used by Alterman and Karal (1968) for the simulation of a single *P*-wave point source in a discrete grid. The analysis is given for the more general heterogeneous formulation, from which the homogeneous formulation is readily obtained by assuming that λ, μ, and ρ are constant.

Consider the heterogeneous elastic wave equation with a compressional line source.

$$(\lambda + 2\mu)\nabla(\nabla \cdot \mathbf{U}_T) - \mu\nabla\times\nabla\times\mathbf{U}_T + \nabla(\lambda + 2\mu)(\nabla \cdot \mathbf{U}_T) - 2\nabla\mu(\nabla \cdot \mathbf{U}_T) + \nabla\mu \times (\nabla\times\mathbf{U}_T) + 2(\nabla\mu\cdot\nabla)\mathbf{U}_T - \rho\frac{\partial^2\mathbf{U}_T}{\partial t^2} = \nabla[-4\pi\ \delta(\mathbf{r} - \mathbf{r}_0)f(t)], \quad \text{(A-1)}$$

where $\mathbf{U}_T$ is the total displacement vector (Karal and Keller, 1959). The right-hand side represents a compressional line source parallel to the z-axis[1], located at $\mathbf{r} = \mathbf{r}_0$ in a cylindrical coordinate system, where $\mathbf{r}$ is the cylindrical radius vector. The function $f(t)$ represents the time variation of the line source. For compactness, the heterogeneous elastic wave equation may be written as

$$\mathbf{L}_H\mathbf{U}_T = \nabla[-4\pi\ \delta(\mathbf{r} - \mathbf{r}_0)f(t)], \quad \text{(A-2)}$$

where $\mathbf{L}_H$ is a linear operator representing the left-hand side of (A-1).

Assume that the elastic material is homogeneous in a region surrounding the source. In this source region (A-1) reduces to

$$(\lambda + 2\mu)\ \nabla(\nabla \cdot \mathbf{V}_T) - \mu\nabla\times\nabla\times\mathbf{V}_T - \rho\frac{\partial^2\mathbf{V}_T}{\partial t^2} = \nabla[-4\pi\ \delta(\mathbf{r} - \mathbf{r}_0)f(t)], \quad \text{(A-3)}$$

[1] This z-axis is not the same as that used in the main text. Rather, this z-axis (and line source) are normal to the plane of the model.

where $\mathbf{V}_T$ represents the total displacement in the source region. This homogeneous equation may be written simply as

$$\mathbf{L}\mathbf{V}_T = \nabla[-4\pi\ \delta(\mathbf{r} - \mathbf{r}_0)f(t)], \quad \text{(A-4)}$$

where $\mathbf{L}$ is the linear operator representing the left-hand side of (A-3).

In the heterogeneous region exterior to the source region, the equation for the total displacement is source free and hence (A-2) may be written as

$$\mathbf{L}_H\mathbf{U}_T = 0. \quad \text{(A-5)}$$

The solution in the exterior region, namely $\mathbf{U}_T$, is coupled to the solution in the source region $\mathbf{V}_T$ by the continuity of displacement and stress at the boundary between the source region and the exterior region. These conditions may be written as

$$\mathbf{U}_T = \mathbf{V}_T \quad \text{(A-6a)}$$

$$\bar{\bar{T}}(\mathbf{U}_T) = \bar{\bar{T}}(\mathbf{V}_T), \quad \text{(A-6b)}$$

where $\bar{\bar{T}}$ represents the total stress dyadic (Morse and Feshbach, 1953, p. 71).

In the source region, the total displacement is defined to be the sum of a source displacement $\mathbf{V}_S$ and a residual displacement $\mathbf{V}_R$, i.e.,

$$\mathbf{V}_T = \mathbf{V}_R + \mathbf{V}_S. \quad \text{(A-7)}$$

By definition, the source displacement is a solution to the equation

$$\mathbf{L}\mathbf{V}_S = \nabla[-4\pi\ \delta(\mathbf{r} - \mathbf{r}_0)f(t)] \quad \text{(A-8a)}$$

subject to the radiation condition at infinity. The residual displacement is a solution to

$$\mathbf{L}\mathbf{V}_R = 0. \quad \text{(A-8b)}$$

The continuity conditions on the boundary of the source region may be written,

$$\mathbf{U}_T = \mathbf{V}_R + \mathbf{V}_S \quad \text{(A-9a)}$$

$$\bar{\bar{T}}(\mathbf{U}_T) = \bar{\bar{T}}(\mathbf{V}_R) + \bar{\bar{T}}(\mathbf{V}_S). \quad \text{(A-9b)}$$

The original equation (A-1) has thus been replaced by the system given by equations (A-5), (A-8), and (A-9). The solutions to the source-free equations, namely (A-5) and (A-8b), may be obtained by finite-difference methods. The solution to (A-8a) will be obtained analytically; from it the source displacement and stress required on the boundary of the source region may be evaluated.

The displacement, due to a compressional line

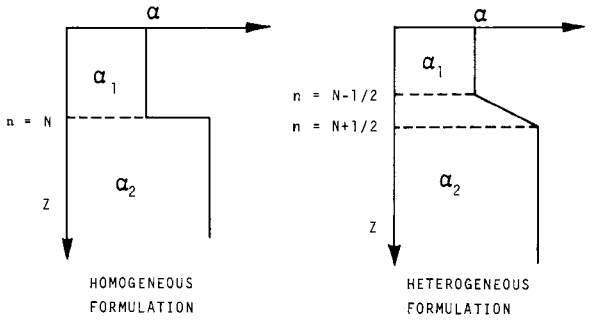

FIG. 8. Velocity transition for the homogeneous and heterogeneous formulations.

source, may be written,

$$\mathbf{V}_S = \nabla\psi_S, \qquad \text{(A-10)}$$

where ψ_S is a longitudinal displacement potential. Substitution in (A-8a) results in the system

$$\nabla^2\psi_S - \frac{1}{\alpha^2}\frac{\partial^2\psi_S}{\partial t^2} = \frac{4\pi}{\alpha^2}\,\delta(\mathbf{r} - \mathbf{r}_0)f(t), \qquad \text{(A-11)}$$

subject to the radiation condition at infinity. The solution to (A-11) (Alford et al, 1974) may be written,

$$\psi_S(\mathbf{r}, t; \mathbf{r}_0) = \frac{1}{2\pi}\int_{-\infty}^{+\infty} i\pi H_0^{(2)}\left(\frac{\omega}{\alpha}\,|\mathbf{r} - \mathbf{r}_0|\right) F(\omega)e^{i\omega t}\,d\omega, \qquad \text{(A-12)}$$

where

$$F(\omega) = \int_{-\infty}^{+\infty} f(t)e^{-i\omega t}\,dt,$$

and $H_0^{(2)}(z)$ is the zero-order Hankel function of the second type. In the present work, the time variation of the line source is assumed to be

$$f(t) = -2\xi(t - t_s)\,e^{-\xi(t-t_s)^2}. \qquad \text{(A-13)}$$

Fourier transformation of this expression yields

$$F(\omega) = -i\pi^{1/2}\,\xi^{1/2}\,\omega e^{\omega^2/4\xi}\,e^{i\omega t_s}, \qquad \text{(A-14)}$$

where t_s is selected such that $f(0) \simeq 0$, and the parameter ξ governs the pulse width.

Substituting (A-12) and (A-14) into (A-10) and performing the differentiation, we obtain

$$\mathbf{V}_S = \mathbf{a}_r\,\frac{1}{2\pi}\int_{-\infty}^{+\infty} \pi^{3/2}\xi^{-1/2}\,\frac{\omega^2}{\alpha^3} H_1^{(2)}\left(\frac{\omega}{\alpha}\,|\mathbf{r} - \mathbf{r}_0|\right)e^{-\omega^2/4\xi}e^{-i\omega t}e^{i\omega t}\,d\omega, \qquad \text{(A-15)}$$

where $H_1^{(2)}(z)$ is the first order Hankel function of the second kind and $\mathbf{a}_r$ is a unit vector in the direction of $(\mathbf{r} - \mathbf{r}_0)$. This Fourier transform is computed numerically to provide the values of the source displacements required in the boundary conditions (A-9). These, in turn, couple the finite-difference solution in the source region $\mathbf{V}_R$ to the solution in the exterior heterogeneous region $\mathbf{U}_T$.

APPENDIX B

DISCREPANCY BETWEEN THE HOMOGENEOUS AND THE HETEROGENEOUS FORMULATIONS

The homogeneous finite-difference formulation requires that the velocities be constant, except at the boundary between regions, where the velocity variation is discontinuous. The heterogeneous finite-difference formulation, on the other hand, treats models which have velocity variation from point to point. We exclude unbounded derivatives of velocity from these models which require continuous velocity variation. If the continuous velocity variation of the heterogeneous formulation is sufficiently abrupt, the theoretical heterogeneous response should approximate the theoretical homogeneous response. We seek an upper bound on the difference between known solutions for the reflection of elastic waves from the discontinuous velocity transition of the homogeneous formulation and the continuous velocity transition of the heterogeneous formulation.

Consider two transition zones with discontinuous and linear velocity variation as a function of depth (see Figure 8). Gupta (1966a) obtained an analytic solution for the reflection coefficient of plane elastic waves reflected from an inhomogeneous linear transition zone for nonnormal incidence. The difference between the homogeneous and the heterogeneous reflection amplitudes depends on the parameter ν, defined as

$$\nu = (2\pi fh)/(\alpha_2 - \alpha_0)$$

or

$$\nu = 2\pi/(G\,\Delta\alpha/\alpha_0),$$

where

f = frequency,
h = thickness of the transition zone,
G = number of grid points per wavelength,

and

$\Delta\alpha/\alpha_0 = (\alpha_2 - \alpha_0)/\alpha_0$ = the fractional change in P-wave velocity.

Figures 2 and 4 of Gupta's study summarize results for a model with a 33 percent velocity contrast. Consider the case corresponding to $\nu = 2$ ($G \simeq 10$) and the case for the abrupt transition ($\nu = 0$). The maximum difference in the PP-reflection coefficient amplitudes is 10 percent, while the maximum difference between the PS-reflection coefficient amplitudes is 15 percent.

The heterogeneous formulation used assumes a model with a continuous velocity transition in which the square of velocity is a linear function of depth [see equation (9) of main text]. The differences of the plane-wave reflection coefficient among several transition zones with continuous velocity and density variation and identical thicknesses and velocity contrasts were considered in Gupta (1966b). The reflection coefficients are essentially identical for all transitions, being independent of the functional form of the velocity and density variation in the transition zone. Hence, the plane-wave reflection coefficient for the heterogeneous formulation would be expected to agree with that for the linear transition zone.

The consideration of the reflection of plane waves is useful as a guide in estimating the size of the amplitude difference between the two formulations. Definitive upper bounds on the amplitude differences between the formulations require an analysis of the reflection amplitudes from a line source, which has not been performed.